

The EF Loop in Green Proteorhodopsin Affects Conformation and Photocycle dynamics

Michaela Mehler,^{†△} Frank Scholz,^{‡△} Sandra J. Ullrich,[†] Jiafei Mao,[†] Markus Braun,[‡] Lynda J. Brown,[§] Richard C. D. Brown,[§] Sarah A. Fiedler,[†] Johanna Becker-Baldus,[†] Josef Wachtveitl,^{†*} and Clemens Glaubitz^{†*}

[†]Institute of Biophysical Chemistry and Centre for Biomolecular Magnetic Resonance and [‡]Institute of Physical and Theoretical Chemistry, Goethe-University Frankfurt, Germany; and [§]Department of Chemistry, University of Southampton, Southampton, United Kingdom

ABSTRACT The proteorhodopsin family consists of retinal proteins of marine bacterial origin with optical properties adjusted to their local environments. For green proteorhodopsin, a highly specific mutation in the EF loop, A178R, has been found to cause a surprisingly large redshift of 20 nm despite its distance from the chromophore. Here, we analyze structural and functional consequences of this EF loop mutation by time-resolved optical spectroscopy and solid-state NMR. We found that the primary photoreaction and the formation of the K-like photo intermediate is almost pH-independent and slower compared to the wild-type, whereas the decay of the K-intermediate is accelerated, suggesting structural changes within the counterion complex upon mutation. The photocycle is significantly elongated mainly due to an enlarged lifetime of late photo intermediates. Multidimensional MAS-NMR reveals mutation-induced chemical shift changes propagating from the EF loop to the chromophore binding pocket, whereas dynamic nuclear polarization-enhanced ¹³C-double quantum MAS-NMR has been used to probe directly the retinylidene conformation. Our data show a modified interaction network between chromophore, Schiff base, and counterion complex explaining the altered optical and kinetic properties. In particular, the mutation-induced distorted structure in the EF loop weakens interactions, which help reorienting helix F during the reprotonation step explaining the slower photocycle. These data lead to the conclusion that the EF loop plays an important role in proton uptake from the cytoplasm but our data also reveal a clear interaction pathway between the EF loop and retinal binding pocket, which might be an evolutionary conserved communication pathway in retinal proteins.

INTRODUCTION

Retinal proteins are photoreactive proteins found in various organisms, enabling light responses such as vision in animals, phototaxis in flagellates, triggering ion channels in algae, and proton pumps in bacteria. All these proteins have a common seven *trans*-membrane helix motif and a retinal cofactor for light reception. The characteristic optical absorption of the retinylidene chromophore is strongly influenced by the protein environment. This bathochromic (opsin) shift compared to retinal protonated Schiff base in methanol ($\lambda_{\text{max.}} = 440$ nm) has been observed in several microbial rhodopsins such as channelrhodopsin-2 ($\lambda_{\text{max.}} = 480$ nm) (1), sensory rhodopsin II ($\lambda_{\text{max.}} = 487$ nm) (2), proteorhodopsin (PR) ($\lambda_{\text{max.}} = 518$ nm) (3), and bacteriorhodopsin (BR) ($\lambda_{\text{max.}} = 568$ nm) (4).

The existence of different opsin shifts shows that mechanisms for color tuning of microbial retinal proteins must exist. This is especially evident in the case of PR, an almost ubiquitous retinal protein occurring in gamma-proteobacteria in the photic zone of the oceans (5). PR has been found to be color tuned with respect to the water depth and two main families, green absorbing PR (GPR) ($\lambda_{\text{max.}} = 525$ nm) close to the surface and blue absorbing PR ($\lambda_{\text{max.}} =$

490 nm) at greater depths, have been identified (6). It is generally accepted that the spectral characteristics of the retinylidene chromophore is strongly affected by its interaction with amino acids located in its direct vicinity. Early reports stated that mainly the distance of the protonated Schiff base from the counterion complex affects its spectral characteristics (7), but interactions with polar and polarizable amino acid residues along the polyene chain, the distortion of the chromophore structure, and the relative orientation of the β -ionine ring to the polyene chain due to steric repulsions within the protein contribute significantly as well (8–12). For example, one single point mutation L105Q in GPR, which is close to the chromophore, shifts the absorption maximum toward blue, whereas the corresponding Q105L mutation in blue absorbing PR causes a green shift (6,13). The recent discovery of a 20 nm redshift of the GPR absorption spectrum upon a single mutation A178R in the EF loop came therefore as a great surprise as the mutation site is far away from the retinylidene (14). This effect is highly position specific and has not been observed in BR (15). Only for halorhodopsin, a similar long-range effect based on a BC-loop mutation has been reported (16). Based on their data and sequence alignments, Kandori and co-workers (17) have suggested that having a small residue such as alanine at position 178 is essential to blueshift the absorption of GPR at neutral pH into a color range compatible with a marine environment.

GPR works as a light-driven proton pump (3) but additional functions have been discussed (18). In addition to

Submitted April 29, 2013, and accepted for publication June 11, 2013.

△ Michaela Mehler and Frank Scholz contributed equally to this work.

*Correspondence: glaubitz@em.uni-frankfurt.de or wveitl@theochem.uni-frankfurt.de

Editor: Daniel Muller.

© 2013 by the Biophysical Society
0006-3495/13/07/0385/13 \$2.00



<http://dx.doi.org/10.1016/j.bpj.2013.06.014>

the color tuning, GPRs have also other unusual molecular properties: The primary proton acceptor D97 has an elevated pK_a due to a pH-dependent coupling to highly conserved H75 (19), which also seems to be involved in proton transfer (20). GPR forms pentamers and hexamers in detergent and lipid bilayers (21,22). The favorable properties of GPR in terms of stability, activity, and spectral resolution have led to an extensive chemical shift assignment and secondary structure analysis by solid-state NMR (23–25). It was also shown that the chromophore assumes an almost 100 percent all-*trans* conformation in ground-state GPR (26). Hydrogen bonding and protonation states of H75 and D97 have been characterized at different pH and reveal a complex interaction pattern, which partially explains the complicated pH dependence of PR's photocycle (19). Solution state NMR has been used to determine backbone structure and dynamic properties of cell free produced GPR within detergent micelles (27,28).

Here, we have resolved the molecular basis of the surprising color shift in GPR_{A178R}. Time-resolved optical spectroscopy has been applied to show that the A178R mutation also affects significantly the kinetics of the primary photoreaction and elongates the duration of the photocycle by a factor of 10. Using solid-state NMR, we have identified mutation-induced structural changes based on chemical shift perturbations. Dynamic nuclear polarization (DNP), a novel hybrid-technique combining electron paramagnetic resonance (EPR) and solid-state NMR to enhance sensitivity of solid-state NMR by orders of magnitude through polarization transfer from stable radicals to nuclei (29), was used to probe retinylidene chromophore and Schiff base conformation. These structural data allow the observed effects on the photocycle dynamics to be explained and reveal a distinct communication pathway between the chromophore and EF loop. Our data indicate that the EF loop plays an essential role for proton uptake in GPR and regulates helical movements during late stages of the photocycle.

MATERIALS AND METHODS

Sample preparation

Samples were essentially prepared as described previously (25): GPR and GPR_{A178R} were cloned in a pET27b(+)-plasmid and expressed in *Escherichia coli* C43-cells. Cells were grown in minimal medium with ¹³C-labeled glucose and ¹⁵NH₄Cl at 37°C. To reduce spectral overlap, amino acids F, L, W, Y, and V were added to the medium to suppress isotope labeling of these residues. When an OD₅₇₈ ~0.7 was reached, 200 mg IPTG and 2 mg retinal dissolved in ethanol were added. Cells were harvested 16–18 h after induction and broken by a Constant System cell disrupter by 1.85 bar. The protein was solubilized in 1.5% *n*-dodecyl-β-D-maltoside (DDM) at 4°C overnight. The solubilized protein (supernatant) was obtained by ultracentrifugation and incubated for 1 h with a Ni-NTA matrix at 4°C. The bound protein was washed and finally eluted with 500 mM imidazole in 0.05% DDM. Purity was checked by absorption spectroscopy and SDS-PAGE (Fig. S1 and Fig. S2 in the Supporting Material).

For optical spectroscopy, GPR and GPR_{A178R} were used solubilized in 0.15% DDM, 150 mM NaCl, 50 mM Tris, pH 6 or pH 9. The sample was diluted to an OD of 0.5 (d = 0.1 cm) for pump-probe spectroscopy and to an OD of 0.7 (d = 1 cm) for flash photolysis.

For solid-state NMR experiments GPR and GPR_{A178R} were reconstituted in DMPC/DMPA (9:1) liposomes in a protein/lipid ratio of 2:1 (w/w). Lipids were resolved in methanol/chloroform (1:2). After evaporation of the solvent, lipids were dissolved in 100 mM NaCl, 50 mM MES, pH 7 and liposomes were formed by passage through a 2 μm pore sized membrane by an extruder with 5–7 bar. Protein and liposomes were mixed slowly and incubated for 0.5 h. Finally, detergent was removed by repeated incubation with biobeads. Proteoliposomes in 50 mM Tris, 5 mM MgCl₂, pH 9 were sedimented by ultracentrifugation for 1 h and packed into a magic-angle spinning (MAS) rotor.

Preparing [14-15-¹³C-all-*trans*-retinal]-PR_{A178R} for DNP-enhanced solid-state NMR

All-*trans* retinal ¹³C-labeled at positions 14 and 15 was synthesized by adaptation of reported procedures (for the synthetic scheme see the Supporting Material) (30). It was incorporated into GPR by adding it to the growth medium as described previously. Reconstituted samples were incubated overnight with 10% H₂O, 30% D₈-Glycerol and 60% D₂O, and 20 mM TOTAPOL (31).

Time-resolved optical spectroscopy

Pump-probe-spectroscopy

A CPA 2001 was used as the laser source operating at a repetition rate of 1 kHz, delivering laser pulses with a central wavelength of 775 nm. The pump-pulse was converted to the absorption maximum using a home-built noncollinear optical parametric amplifier (20 nJ/pulse). Afterward, the pump-pulse was temporally compressed using a prism compressor. The probe-pulse consists of a spectrally broad pulse (white light continuum) and was generated by focusing a part of the laser fundamental into a sapphire crystal. The pump- and probe-pulses were spatially overlapped in the sample and the probe-pulse was detected on a photodiode array with a spectral resolution of Δλ_{res.} = 4 nm. The time resolution varied between 50 and 90 fs.

Flash photolysis

The samples were excited at the particular absorption maximum (pulse width: 20 ns; intensity: 3 mJ/cm²). The laser pulses were generated using an optical parametric oscillator (OPO, GWU Laser Technics) that is pumped by the frequency tripled of a Nd:YAG laser (Spotlight 600 Innolas Laser GmbH). For the probe beam the output of a xenon lamp (LC8; Hamamatsu) is guided through a monochromator (Photon Technologies International) for wavelength selection. Afterward, this beam is focused into a fused quartz cuvette (d = 1 cm) and guided through a second monochromator to get rid of scattering light, due to laser excitation. The probe beam is detected by a photomultiplier tube (Photosensor H6780-02, Hamamatsu) and analyzed by a digital storage oscilloscope (LeCroy, Waverunner 62 Xi).

Simulation of the transient data

The flash photolysis data were fitted to a reaction scheme that was slightly altered compared to an earlier one proposed by Varo et al. (32). The following reaction sequence was assumed: K ⇌ M₁ → M₂ ⇌ N₁ ⇌ N₂ ⇌ PR(O) → PR. The spectra of M₁ and M₂, as well as PR(O) and PR are assumed to be equal. A Levenberg-Marquardt algorithm was used to calculate photointermediate rate constants and absorption spectra using data from Varo et al. as starting values (32). The system of linear differential equations is solved numerically.

Solid-state NMR experiments

DNP-enhanced MAS-NMR

Experiments were performed on a Bruker Avance II 393 MHz spectrometer equipped with a modified Bruker 3.2 mm low-temperature probehead and connected to a 259 GHz gyrotron (Gycom, Russia). The effective microwave power applied to our NMR samples was ~ 2 W. A sample of [14-15- ^{13}C -all-*trans*-retinal]-GPR_{A178R} (~ 2 mg) was packed into a 3.2 mm ZrO₂ rotor and sealed with a homemade tapered rubber disk. The rotor was closed by a Vespel cap and flash frozen in liquid nitrogen before inserting it into the low-temperature probehead. For all measurements, a MAS frequency of 8000 ± 2 Hz was used. The temperature inside the MAS rotor was kept at 103.0 ± 0.2 K. All DNP experiments started from a ^1H hard pulse (2.2 μs) followed by ^1H - ^{13}C cross-polarization (CP) with a contact time of 400 μs and ^1H and ^{13}C spin lock fields of 56.8 and 65.4 kHz, respectively. The POST-C7 scheme was used for exciting and reconverting DQ (double-quantum) coherence (33). A continuous wave decoupling at 112 kHz and a SPINAL64 (34) decoupling at 105 kHz were applied during POST-C7 pulses and acquisition time, respectively. HCCH torsion angles were measured by separated local field (SLF) experiments, essentially as described by Levitt and co-workers (35): DQ coherences are excited, evolve under homonuclear proton decoupling, and are detected after a reconversion step. Here, two complete POST-C7 cycles were used for both DQ excitation and reconversion. A PMLG (phase modulated Lee-Goldburg) homonuclear decoupling step (36) with an RF field of 112 kHz was applied during the DQ-evolution time, which was incremented by multiple integers of 18 PMLG cycles (1/9th of one rotor period). Two equal cw proton-decoupling periods (112 kHz) were applied before and after the evolution time to keep the total evolution time constant (two rotor periods, 250 μs). The simulation of spin dynamics was performed with SIMPSON (37).

Multidimensional MAS-NMR experiments for identifying chemical shift changes

All MAS-NMR experiments were conducted using a 3.2 mm triple-resonance DVT HCN probehead on a Bruker wide bore Avance III solid-state NMR spectrometer with ^1H frequency of 850.32 MHz. A sample spinning rate of 14 kHz and SPINAL64 proton decoupling of 83 kHz was used during evolution and acquisition. Typical ^1H and ^{13}C 90° pulse lengths were 3 and 4 μsec , respectively. For all experiments the acquisition time in the direct dimension was 20 ms and sample temperature was set to 270 K. ^{13}C and ^{15}N chemical shift referencing was carried out with respect to DSS through Alanine (179.85 ppm). ^{13}C - ^{13}C correlation spectra were acquired using proton-driven spin diffusion (PDSD) (see Fig. 3) with a mixing time of 20 ms. A CP contact time of 1.5 ms and a 2.5 sec recycle delay time were used. The acquisition time was set to 10 ms in the indirect dimen-

sion and 1024 increments with 80 scans each were recorded. For NCA/NCO/NCACX/NCOCX experiments, initial magnetization was created by a ^1H - ^{15}N CP step of 1.25 ms. A recycle delay of 3 s was used. Specific CP with a 90–100 linear ramp on the ^{13}C channel was used to create ^{13}C magnetization from ^{15}N using a contact time of 3.5 ms and 5 ms for NCO and NCA transfer, respectively. For NCACX and NCOCX spectra, a 30 ms dipolar-assisted rotational resonance mixing step was used for ^{13}C - ^{13}C transfers. Spectra of wild-type (WT) GPR were assigned using published chemical shift data (23). Comparing the PDSD, NCA, and NCO spectra of GPR_{A178R} with GPR data enabled identifying significant chemical shift changes. Peak assignment was confirmed using the NCACX and NCOCX spectra. Data analysis was done using TOPSPIN 2.1 and CCPN 2.2.2.

RESULTS

UV/Vis spectroscopy

A series of pH-dependent absorption spectra of GPR and GPR_{A178R} solubilized in DDM have been recorded (Fig. 1, A–C). The absorption maximum λ_{\max} depends on the protonation state of the primary proton acceptor D97 (38). For PR, λ_{\max} shifts from 520 to 540 nm when lowering the pH from 9 to 6. GPR_{A178R} follows this trend but shows a significant redshift with changes from 533 to 550 nm within the studied pH range (Fig. 1, A and B). The pK_a of D97 can be obtained from the inflection point of the sigmoidal titration curves and was found at 7.0 for GPR and 7.7 for GPR_{A178R} (Fig. 1 C). These data agree with those reported by Kandori and co-workers (17) for a cysteine-less mutant of GPR in which the A178R mutation was introduced.

Solid-state NMR on GPR_{A178R}

Solid-state NMR experiments on GPR_{A178R} reconstituted into DMPC/DMPA lipid bilayers have been carried out to probe structural effects of the A178R EF loop mutation onto Schiff base environment, retinylidene conformation, and protein structure.

The ^{15}N chemical shift of the protonated Schiff base at pH 9 is not affected by the A178R mutation (Fig. S3), but a

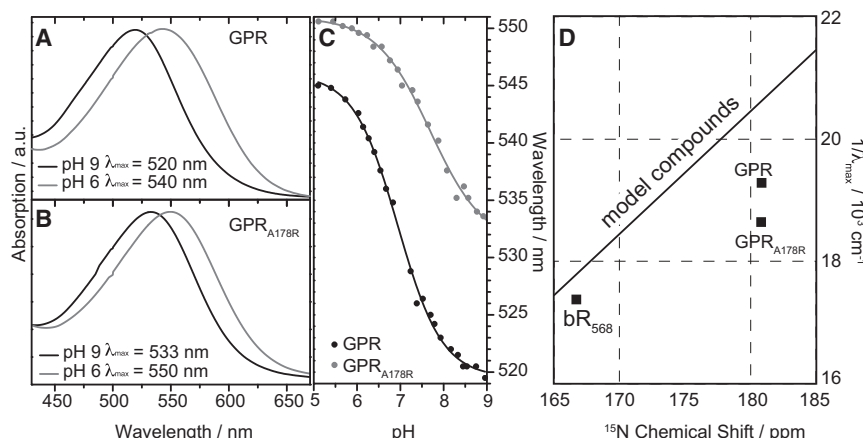


FIGURE 1 pH-dependent stationary absorption spectra of GPR (A) and GPR_{A178R} (B). The single point mutation A178R causes a general redshift of up to 13 nm (14). The pK_a of the primary proton acceptor (C). Correlation between λ_{\max} and ^{15}N chemical shifts of the pSB obtained from retinal derivatives with all-*trans* polyene chains with different halide counterions (39) in comparison to GPR and GPR_{A178R} (D). The mutant deviates more from model behavior than GPR. ^{15}N -MAS NMR spectra are shown in Fig. S3.

comparison with the corresponding values from Schiff base—counter ion model complexes and their correlation with λ_{\max} shows that GPR_{A178R} deviates from model behavior more than GPR (Fig. 1 D) (39).

To probe mutation-induced effects on the chromophore itself, we have incorporated 14-15-¹³C-all-*trans* retinal into GPR_{A178R} ([14-15-¹³C-retinal]-GPR_{A178R}). Retinal ¹³C chemical shifts are sensitive indicators for conformational changes. In particular, double quantum spectroscopy has been shown to offer unique insight: Chemical shift data can be extracted more easily by natural background suppression and CC bond lengths and HCCH torsion angles can be obtained from DQ built-up curves (40) and SLF experiments (35). Such experiments will also benefit from signal enhancement provided by DNP (29). DNP-enhanced DQ filtered ¹³C spectra are shown in Fig. 2 A. A DNP enhancement of 20 (microwave on/off) was obtained, which accelerates data acquisition 400-fold. Both peaks, C14 and C15, appear broader than in GPR and are slightly shifted. C14 is detected at 122.1 ppm (120.2 ppm in GPR) and C15 at 160.7 ppm (161.7 ppm in GPR). A small additional subpopulation is observed at 111 and 165 ppm, which is not detectable in WT GPR. The evolution of DQ coherences between C14 and C15 over two rotor periods (including a centering π -pulse) under homonuclear proton decoupling is shown in Fig. 2 B. Simulations illustrate that the evolution curve depends on the HCCH torsion angle around the C14-C15 bond, but our data show that it remains almost unchanged in GPR_{A178R} compared to GPR (161°).

The observed effects on color and retinylidene chemical shifts must be induced by structural changes triggered by the EF loop and transferred through the protein into the retinal binding pocket. We have therefore analyzed mutation-induced ¹³C and ¹⁵N chemical shift perturbations by comparing CC, NCA, and NCO spectra of GPR_{A178R} with those obtained from GPR. Samples were uniformly ¹³C and ¹⁵N labeled except for amino acids F, L, W, Y, and V to reduce spectral overlap. In a first step, peaks shifted upon mutation were identified and tentatively assigned based on published chemical shift assignment (23). In a second step, assignments were supported by two-dimensional NCOCX/NCACX experiments on GPR and GPR_{A178R}. We found 63 residues in which either backbone and/or side-chain resonances show chemical shift changes larger than 0.2 ppm (Table S1). A CC correlation spectrum (¹³C-¹³C-PDSD) of GPR and GPR_{A178R} is shown in Fig. 3. This experiment displays through-space correlations but a short mixing time of 20 ms was used emphasizing spin-spin distances in the range of single bonds. A number of crosspeaks shift upon mutation such as D97 (Fig. 3 B) and D227 (Fig. 3 C) or A115, 116, 143, 168, 174, and 178 (Fig. 3 D). Altogether, 31 affected residues can be identified from this spectrum. Changes mainly in CA-CB crosspeaks are detected but in 11 cases, chemical shift perturbations in side chains were monitored as well. These data are com-

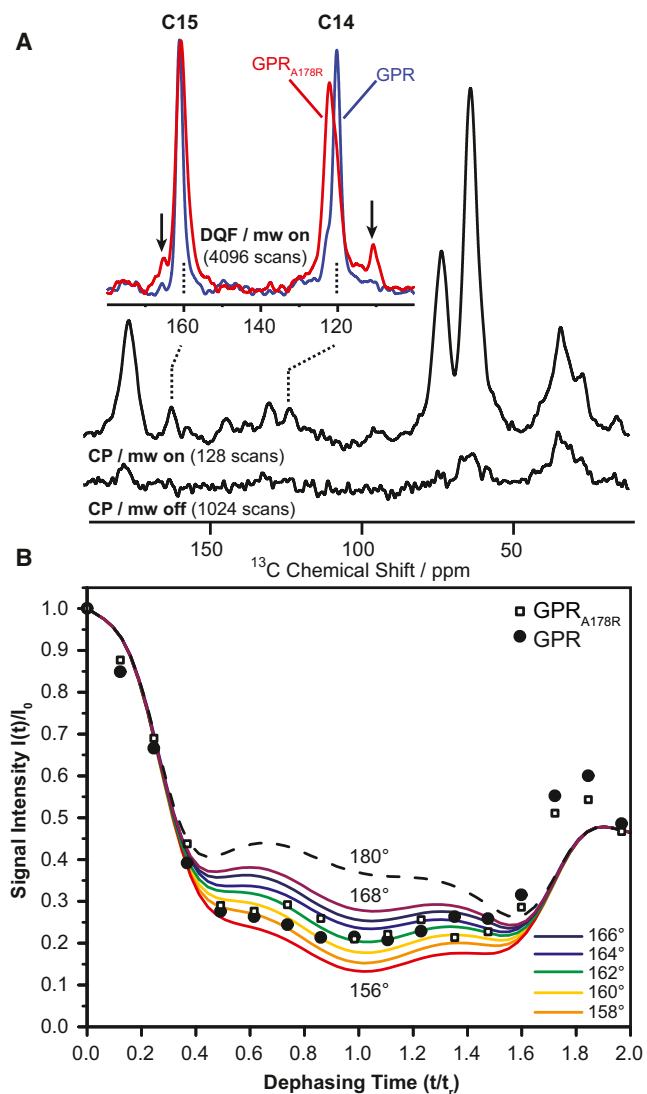


FIGURE 2 DNP-enhanced ¹³C-CP MAS NMR spectra of 14-15-¹³C-all-*trans*-retinal GPR and GPR_{A178R} (A). Using DNP, a 20-fold signal enhancement is achieved at 100 K. ¹³C natural abundance is suppressed by double-quantum filtering. In GPR, the ¹³C chemical shifts of C14 and C15 are found at 120.2 and 161.1 ppm and change in GPR_{A178R} to 122.1 and 160.7 ppm, respectively. The linewidth increases from 160 to 290 Hz. In GPR_{A178R}, small additional peaks at 110.7 and 165.6 ppm are detected (arrows). The HCCH torsion angle at position C₁₄-C₁₅ has been determined by DQ-SLF experiments (B). Experimental and simulated DQ signal intensities under homonuclear decoupling are plotted as a function of time t in units of rotor periods t_r and reveal a torsion angle of 161° in GPR_{A178R}, which is similar to GPR. Further details are given in the Materials and Methods section.

plemented by NCA (Fig. S4) and NCO (Fig. S5) spectra, which confirmed our findings from Fig. 3 and also allowed identification of an additional 32 chemical shift perturbations. The location of all affected residues is plotted in a topology diagram (see Fig. 7). The observed chemical shift perturbations progress from the mutation site in the EF loop through helices E and F into all other helices as well as into the BC and DE loops.

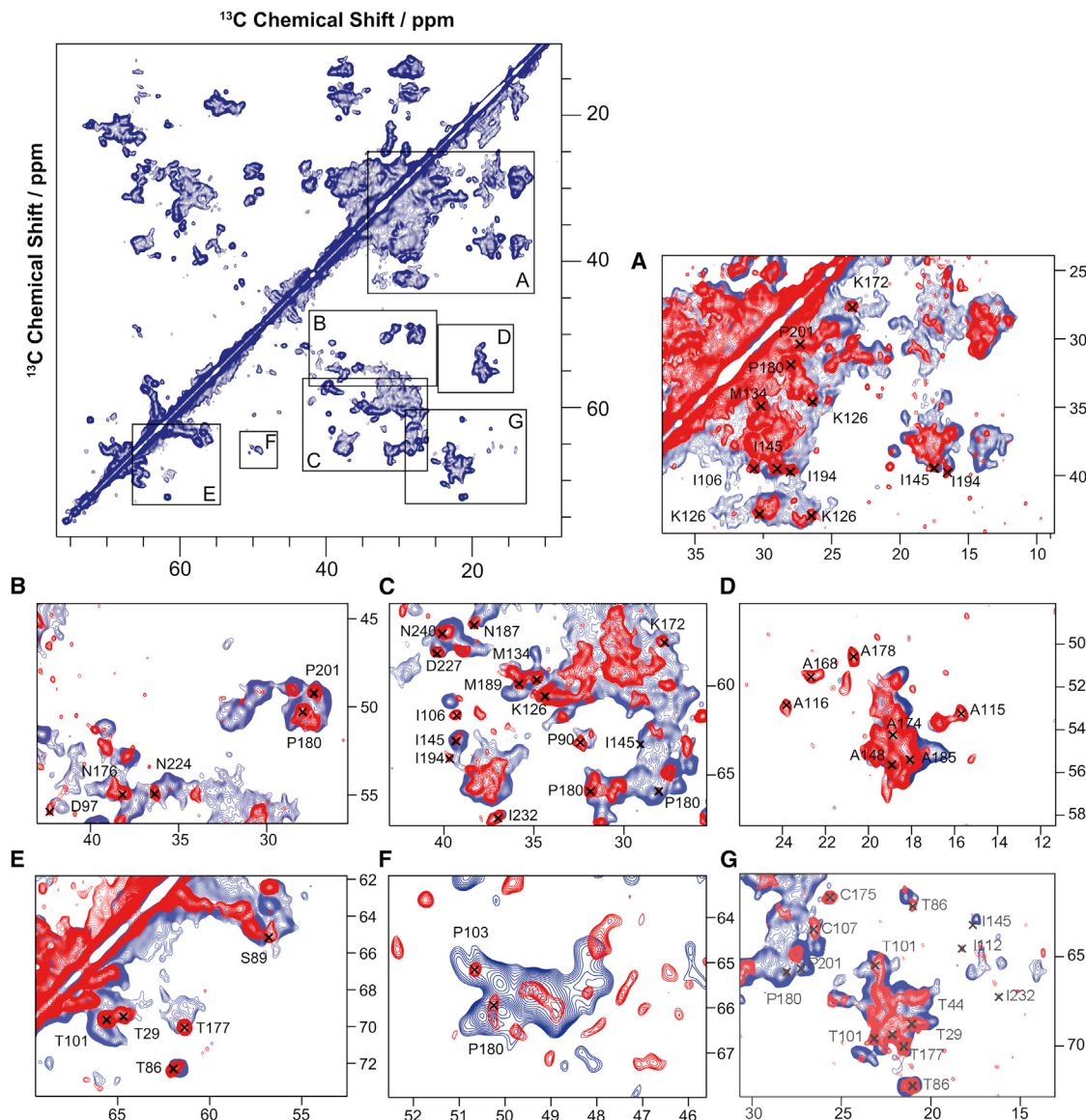


FIGURE 3 ^{13}C - ^{13}C -PDSD spectra of GPR (red) and GPR_{A178R} (blue) at pH 9 reconstituted in lipid bilayers. A mixing time of 20 ms was used. A large number of chemical shift differences can be identified as highlighted in the regions A–G. Affected are for example D97 (B) and D227 (C) and alanines in the C-helix and EF loop (D). Chemical shift changes were also identified in NCA and NCO spectra (Fig. S4 and Fig. S5) and resonance assignment was verified by NCOCX and NCACX experiments. A complete list of chemical shift changes is given in Table S1 and highlighted in the topology plot shown in Fig. 7 and in the 3D structure model in Fig. 8.

Probing the primary reaction in GPR_{A178R} by pump-probe spectroscopy

Our solid-state NMR data show remarkable structural effects on the photoactive site caused by the distant EF loop. We have therefore probed its consequences for the dynamics of the primary photoreaction by time-resolved optical pump-probe spectroscopy in the ps - ns time range. The photoisomerization around the C13-C14 double bond and the formation of the first ground state intermediate (K intermediate in the photocycle of BR) occur on this timescale. For BR and GPR it is well known that these processes are

very sensitive toward the structural environment of the primary proton acceptor (D85 in BR, D97 in GPR) (41–44).

The photoexcitation-induced time-resolved absorbance changes in GPR_{A178R} are compared to data obtained for GPR as reported earlier (44,45) (Fig. 4). Experiments were performed at pH 6 and pH 9, which is below and above the pK_a of the primary proton acceptor. For GPR at alkaline pH, four spectral features can be observed. These regions can be attributed to the absorption of the excited state, the stimulated emission, the depletion of the ground state, and the absorption of the photoproduct. All spectral features

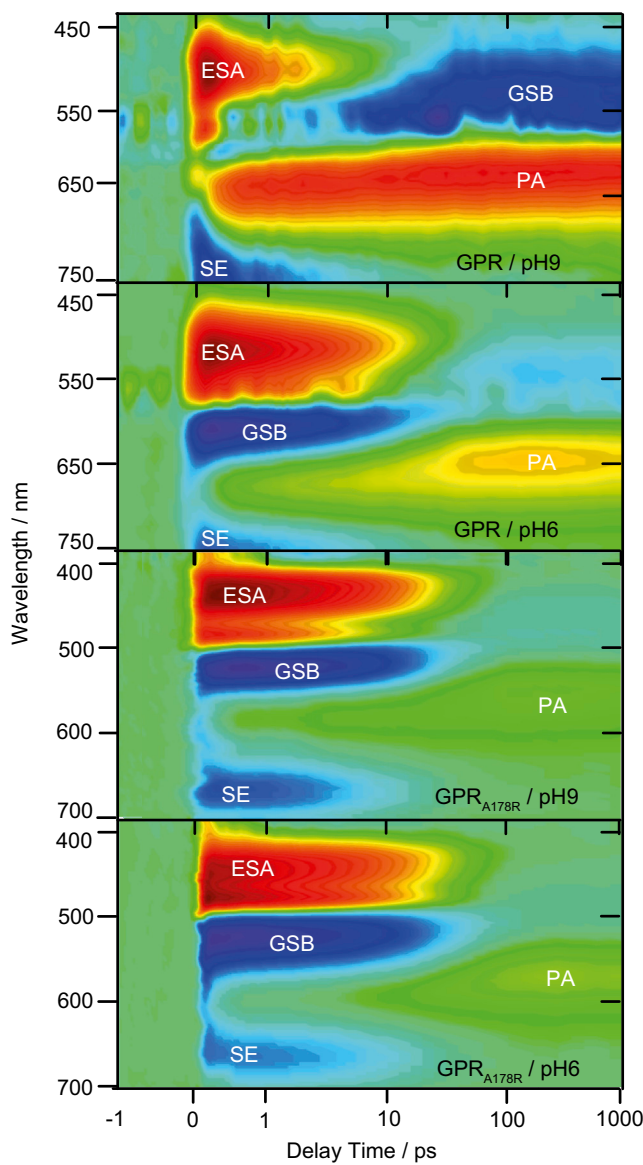


FIGURE 4 Transient absorption changes of GPR compared to GPR_{A178R} at pH 6 and pH 9 after photoexcitation at their particular absorption maximum. The time axis is scaled linear until 1 ps and logarithmic until 1 ns. The amplitudes are color-coded: red indicates a positive absorption, blue negative, and green marks areas where no absorption change could be detected. Abbreviations: ESA (excited state absorption), GSB (ground state bleach), PA (photoinduced absorption), and SE (stimulated emission). Individual time traces at 451, 579, and 707 nm are given in Fig. S6. Time constants obtained via a global fit analysis are given in Table 1.

are redshifted for GPR_{A178R} according to the bathochromic shift observed in the stationary absorption spectrum (Fig. 1). The primary reaction is significantly prolonged for the GPR_{A178R} mutant illustrated by the lifetime of the S₁-state, represented by the decay of the excited state and stimulated emission (for a comparison of the temporal evolution of the different spectral features see also the single transients at distinct probe wavelengths in Fig S6). However, the amplitude of the photoproduct at longer delay times is lower

for GPR_{A178R}, suggesting either a reduced quantum yield for photoisomerization or extinction coefficient of the photoproduct.

The transient data set is simulated by a global fit analysis consisting of a sum of exponential decays convoluted with the instrument response function. The time constants for all wavelengths are the same, whereas the amplitudes are varied (Table 1). The corresponding decay-associated spectra are plotted in Fig. S7. The global fit analysis reveals four time constants for the GPR and an additional time constant τ_x for GPR_{A178R}. The time constants can be assigned to similar processes described for GPR earlier (44,45). τ_1 describes the motion of the initially generated wave packet out of the Franck-Condon region and contains contributions from stimulated emission and excited state population, respectively. τ_x can be assigned to the same processes as τ_1 (see the Supporting Material). The time constants τ_2 and τ_3 can be assigned to the decay of the excited state population.

Obviously, the mechanism of photoisomerization seems to be affected upon A178R mutation. For GPR, the corresponding time constants τ_2 and τ_3 exhibit similar amplitude spectra suggesting that the initial and final states of these transitions are equal (45). In contrast, the amplitude spectra of τ_2 and τ_3 obtained for GPR_{A178R} differ significantly, illustrating that τ_2 and τ_3 describe different reaction paths on the S₁ potential energy surface. Moreover, the ratio of the amplitudes is similar at both pH-values, whereas for GPR it was shown that at alkaline pH the faster reaction channel is preferred.

The obtained time constants in Table 1 confirm that all processes are prolonged for GPR_{A178R}. The comparison of the obtained time constants and the corresponding decay-associated spectra at different pH for GPR and GPR_{A178R} suggests that photoisomerization becomes nearly pH-independent in GPR_{A178R}. For GPR, τ_2 is increased by a factor of 3 and τ_3 by a factor of 2 upon lowering the pH from 9 to 6. In contrast to this the obtained time constants are similar for GPR_{A178R} at both pH-values. Only for τ_3 a small but significant increase can be observed upon lowering the

TABLE 1 Global fit analyses of the data set shown in Fig. 4

	τ_1/ps	τ_x/ps	τ_2/ps	τ_3/ps	τ_4
GPR/pH 6.4	0.15	—	1	16.2	∞
GPR/pH 9	0.14	—	0.28	9.5	∞
GPR _{A178R} /pH 6	<0.1	0.6	3.7	24	∞
GPR _{A178R} /pH 9	<0.1	0.7	3.6	20	∞

The data in Fig. 4 were analyzed by a global fit routine using a sum of exponentials with the same time constants for all wavelengths but different amplitudes. As reported earlier (19,44), the primary reaction in GPR can be described by four time constants (τ_1 – τ_4), whereas one additional constant (τ_x) was needed for GPR_{A178R}. Furthermore, a time constant that is set to infinite is necessary to describe the constant amplitude for longer delay times. This time constant represents the difference spectrum between the first photointermediate and the initial state.

pH from 9 to 6. Again, the effect is not as pronounced as for the WT GPR.

Probing the photocycle in GPR_{A178R} by flash photolysis

Our solid-state NMR data show mutation-inducing effects at the retinylidene but also on residues such as D97, which are directly involved in proton transfer. We have therefore analyzed mutation-induced alterations in the photocycle dynamics after photoexcitation on a timescale of 1 μ s to 10 s. Transient absorption changes for GPR and GPR_{A178R} after photoexcitation are shown in Fig. 5.

At 590 nm, a decrease of the positive absorption signal in GPR is observed due to the decay of the K-intermediate, which is the photoproduct of the primary reaction observed in the pump-probe measurements discussed previously. This decay is accompanied by an increasing absorption monitored at 400 nm typically found for a deprotonated Schiff base species (M-intermediate). The M-intermediate is followed by an absorption increase at 590 nm, caused by the formation of late N/O-intermediates. These species decay simultaneously with the growth of the signal at 500 nm arising from the repopulation of the initial state. The GPR photocycle is completed within hundreds of ms. In contrast, the photodynamics of GPR_{A178R} is strongly altered: The K-intermediate has almost completely decayed after 1 μ s, whereas at the same time the M-state at 400 nm appears already completely populated. The subsequent formation of the N/O-intermediates at 590 nm and the repopulation

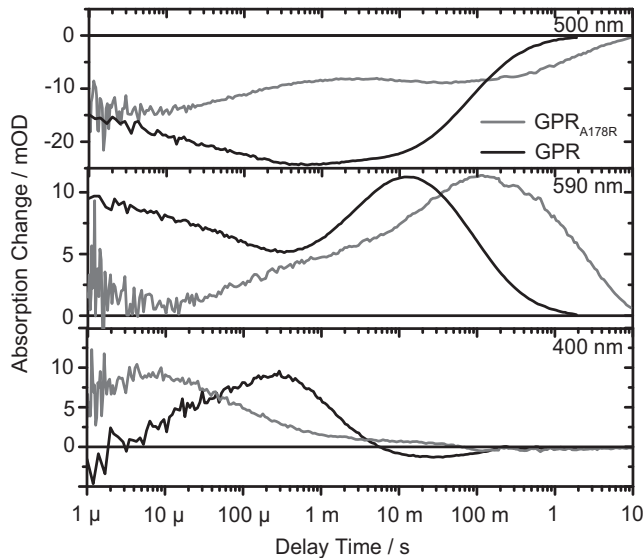


FIGURE 5 Laser-flash-induced transient absorption changes at pH 9 for GPR_{A178R} and GPR. The transients are representative for the dynamics of the ground state population (500 nm), the K-decay at early delay times and the formation of the N/O-intermediates at late delay times (590 nm) and the formation and decay of the M-intermediate (400 nm). Time constants obtained via a global fit analysis are given in Table S2.

of the initial state monitored at 500 nm are delayed compared to GPR.

We have analyzed the transient data set using a reaction scheme proposed earlier (32). However, an additional photointermediate was necessary to satisfactorily simulate the experimental data. The additional photointermediate is populated with a time constant of 48 ms. Considering the obviously multiexponential rise of the transient monitored at 590 nm in Fig. 5, the additional intermediate is attributed to an interconversion of several N-intermediates (termed N₁ and N₂). Fig. 6 shows an overview of the photocycle dynamics of GPR and GPR_{A178R}. The decay of the K-intermediate and the formation of the M-intermediate are dramatically accelerated for GPR_{A178R}. In contrast to this the later steps of the photocycle, mainly the lifetimes of the N₁, N₂, and O intermediate are prolonged, leading to an overall photocycle duration, that is 10-fold higher for

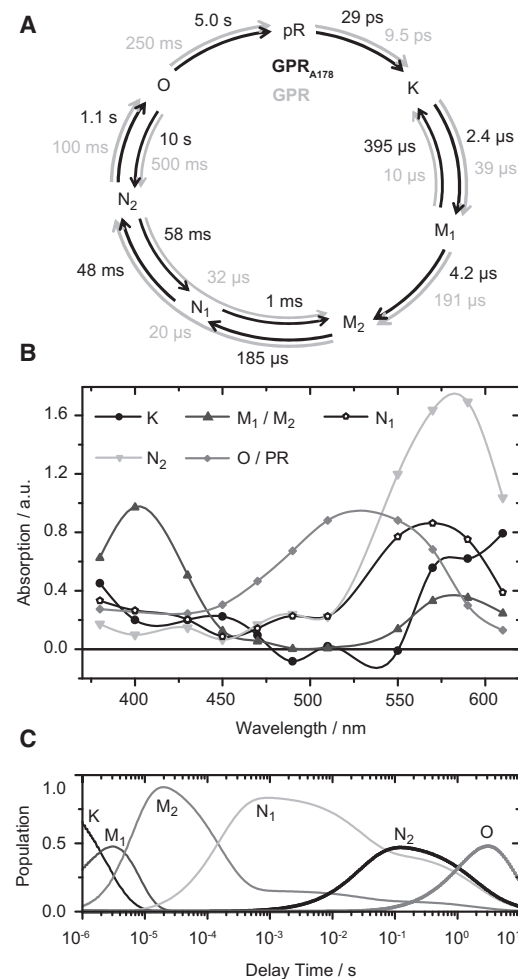


FIGURE 6 The experimental data is fitted to a reaction scheme described in the Materials and Methods (A). For simulating our experimental data we have varied the extinction coefficients of the photointermediates (B) and the time-dependent population changes (C). Multiplying the time-dependent population changes and the extinction coefficients reestablishes the experimental data obtained by flash photolysis.

GPR_{A178R} compared to GPR. Fig. 6 also contains the time-dependent population changes of the different intermediates, as well as the calculated absorption spectra of the different intermediates. The N₁ to N₂ interconversion is accompanied by a small bathochromic shift and an increase of the extinction coefficient.

DISCUSSION

Kandori and co-workers (14) have shown that a single mutation A178R in the EF loop of GPR, which is far away from the retinal binding site, causes a surprisingly large redshift and changes the pK_a of the primary proton acceptor D97 (Fig. 1). They have also shown that this effect is strongly position dependent (15) and depends merely on the side-chain volume and less on the charge of the amino acid at position 178 (17). Here, we demonstrate that this mutation not only causes a redshift but also significantly modulates the photocycle dynamics of GPR. The photoisomerization is prolonged and nearly independent on pH. The latter is surprising because it was shown that this process is twofold accelerated at alkaline pH compared to acidic pH. Overall, the photocycle takes ~10 times longer due to a longer lifetime of the N/O intermediate. In the following, we will explain the molecular basis for these surprising effects based on our solid-state NMR data.

We have identified mutation-induced chemical shift changes in 63 residues spread out across the protein sequence as illustrated in the topology plot in Fig. 7. Affected residues are found in all seven helices and in the BC, DE, and EF loops. The location of these residues is

visualized in a structural model of GPR in Fig. 8 A. Replacing A178 with R in the EF loop triggers chemical shift changes, which progress from the EF loop through helices E and F across the whole protein. The chemical shifts of resonances arising from CA, CO, CB, and N sites in the protein backbone depend on dihedral angle Φ and Ψ and alterations indicate small structural changes.

It seems that incorporating a larger side-chain volume at position 178 (Arg is twice as large as Ala) disrupts the EF loop with consequences for the whole GPR structure including the retinal binding pocket and subsequently also photocycle dynamics. Kandori and co-workers had already speculated that the EF loop must contain specific structural elements, which are disturbed upon mutation. Indeed, a previous solid-state NMR study by Brown, Ladizhanski and co-workers has identified a kink at the cytoplasmatic end of helix E at positions A168 and G169 preceding a short α -helix E'170-N176 (E'), which is followed by a β -turn formed by T177, A178, and S179 (23). The existence of a kink at position G169 and the helical segment E' was later also observed in the 3D backbone structure of cell-free produced GPR determined by liquid-state NMR in DHPC micelles (27) and is also consistent with EPR/DNP studies (46). Interestingly, a structured EF loop is not exclusive to GPR but is also found in other retinal proteins and GPCRs (47–51). Our data clearly show that the NMR signals of almost all residues between A168 and S179 in this kink-helix- β -turn region are affected by the A178R mutation: We have identified chemical shift changes larger than 0.2 ppm for A168, G169, E170, G171, K172, S173, A174, C175, N176, and P180 (Table S1). The CA chemical shift

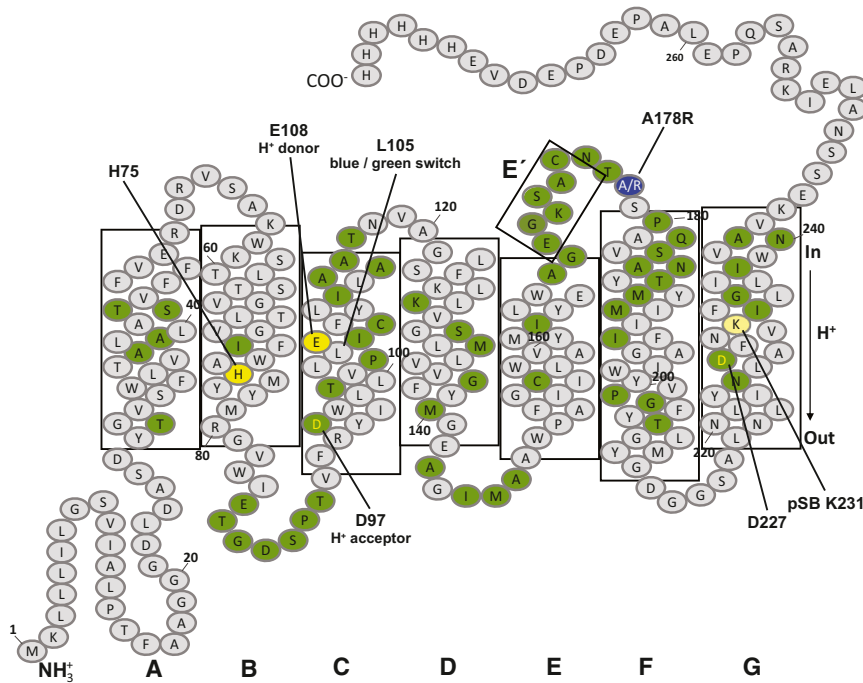


FIGURE 7 The A178R mutation in the EF loop induces backbone and/or side-chain chemical shift changes in 63 residues (colored dark, see also Fig. 3, Fig. S4, Fig. S5, and Table S1). They are located in all seven helices as well as in the BC, DE, and EF loops. Residues of direct functional relevance are labeled. The EF loop contains a short interfacial helix E' followed by a turn structure (23,27).

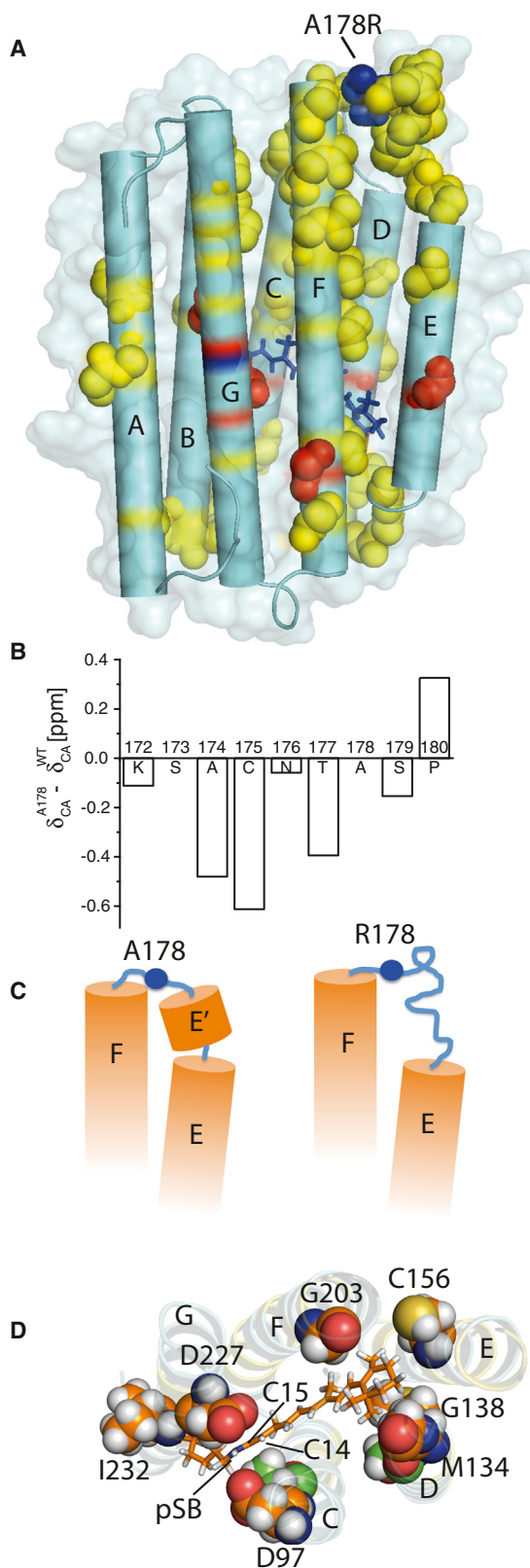


FIGURE 8 Residues for which mutation-induced chemical shift changes are observed and are highlighted in a simplified structure model, which is consistent with NMR data and based on homology to BR (19,24,25,27,65) (A). An interaction pathway from the EF loop to the retinal

differences are shown in Fig. 8 B and reveal a trend toward smaller values upon mutation indicating a distortion of the E' helical structure between residues 168 and 179 as illustrated in the cartoon in Fig. 8 C. This loosened loop structure must trigger structural and dynamic changes in GPR explaining the observed color shift and altered photocycle dynamics.

In or close to the retinal binding pocket, we have identified seven residues, which show clear chemical shift changes larger than 0.2 ppm (Fig. 8 A, color-coded in red). These are D97, M134, G138, C156, G203, D227, and I232. Fig. 8 C shows the approximate location of those seven residues with respect to the retinal. The primary proton acceptor D97 and residue D227 are located on both sides of the retinal polyene chain, close to C14, C15, and the protonated Schiff base. The pSB ^{15}N resonance is not affected, whereas the ^{13}C chemical shifts of retinal carbons C14 and C15 move by +1.9 and -0.4 ppm, respectively, upon mutation. D97 is considered as primary counterion of the protonated Schiff base and has a strong influence on the photokinetics either for the ultrafast timescales (from femtoseconds to 1 ns) (44,45) or on the later stages of the photocycle (1 μs to 1 s) (3,32,52). Residue D227 has been suggested to play a role in the photocycle and retinylidene isomerization (53).

Our observations allow the unusual redshift in GPR_{A178R} to be explained. The chemical shift changes in the retinylidene polyene chain indicate alterations in pSB/counterion distances and relative orientation. A weakening of pSB/counterion association has been shown to shift retinal absorption maxima to longer wavelengths (54). Another contribution could be a change in the β -ionone ring/polyene chain coplanarity, which is mainly caused by protein-retinal contacts and contributes 20% to the opsin shift of BR (12). Direct structural changes within the polyene chain around C14 and C15 are not observed, as the HCCH torsion angle remains almost unaltered compared to the WT (Fig. 2). However, residues for which chemical shift changes have been observed surround the β -ionone ring. Therefore, the ring-protein interaction interface is altered, which could result in altered ring orientation and subsequent color change.

Restructuring effects of the retinal binding pocket also agree with the different pK_a of D97 in the main titration curve (Fig. 1) and the loss of pH dependence of the primary reaction, which is also 2.5-fold slower. In GPR, pH affects

binding pocket can be envisaged. The observed chemical shift changes (B) indicate that the secondary structure in the EF loop is distorted (C). A number of seven residues out of 63 affected by the A178R mutation (Fig. 7) are directly located within or close to the retinal binding pocket (D). These include G203, C156, M134, and G138 in close proximity to the retinal ring as well as the primary proton acceptor D97. D227 is assumed to play a role in retinal isomerization. Chemical shift changes within these residues indicated slight structural rearrangements, which can explain the significant mutation-induced changes in GPR's optical and kinetic properties.

the protonation state of the primary proton acceptor leading to a spectral shift in the absorption spectrum of the initial state (38) and a strong pH-dependent isomerization rate (44,45). In general, it is known that the first electronic state S_1 exhibits a more pronounced charge-transfer character than the ground state S_0 . The transition into the first electronic state S_1 is accompanied by an increase of the dipole moment (55) that was estimated to be 12 D (56). Theoretical studies revealed that electrons are shifted from the hydrocarbon tail toward the protonated Schiff base upon photoexcitation (57–59). Therefore, a negative charge placed in the vicinity of the Schiff base influences the electronic configuration of the retinal. The relative orientation of the primary proton acceptor to the Schiff base can therefore stabilize or destabilize the S_1 and the S_0 state. This directly affects the absorption maximum of the retinal, which reflects the energetic difference between the S_1 and the S_0 state. For GPR_{A178R} a pH-dependent shift of the absorption maximum can be observed indicating that the electronic configuration of the retinal is affected by an either protonated or deprotonated primary proton acceptor D97. However, pump-probe spectroscopy reveals that the protonation state of D97 has nearly no influence on the photoisomerization process. For BR (60), GPR (44), and ChR2 (61), it was shown that a primary proton acceptor functions as an efficient catalyst for photoisomerization, which is not the case in GPR_{A178R}. It is known from quantum mechanical calculations that the slopes on the S_1 potential energy surfaces of the S_1 state are significantly affected by the relative orientation of an acetate residue with respect to the protonated Schiff base resulting in altered isomerization rates (62). A steeper slope on the S_1 -potential energy surface leads to an accelerated relaxation from the Franck-Condon region to the S_1/S_0 conical intersection, therefore accelerating the decay of the S_1 -state (62). These findings support that the A178R mutation strongly affects the position of D97 with respect to the chromophore, which is also supported by our NMR data. D97 adopts a position in which the effect of deprotonation on the S_1 potential surface is nearly absent.

Our ^{13}C -DNP MAS NMR data show a small 13-*cis* subpopulation in GPR_{A178R} in contrast to GPR (Fig. 2). Isomerization control in GPR has been linked to residue D227 (53,63), which is located in close proximity to the chromophore and is directly affected by the A178R mutation. A structural change in the retinal binding pocket could reduce the isomerization control of this residue. For example, it has been shown that PR_{D227N} contains larger amounts of 13-*cis* retinal in its ground state and exhibits only minimal pH dependence for the primary reaction and a prolonged photocycle in contrast to GPR (64). Similar observations are made here. This means that restructuring the retinal binding pocket involves altered distances between Schiff base, retinal, and counterions including alteration in the hydrogen bonding network.

As discussed previously, the EF loop structure is distorted in GPR_{A178R} resulting probably in weaker structured constraints of the EF loop onto helices E and F. Hence, structural changes propagate through both helices via DE and FG loops, via side-chain contacts, and through retinal-protein contacts to the rest of the protein (Fig. 8 A). The altered structure in the EF loop must also have consequences for the photocycle steps involving movements of helices E and F. The EF loop structures could restrain helix movements during the photocycle, which become more relaxed in the mutant. Indeed, the A178R mutation slows down the photocycle 10-fold despite the accelerated decay of the K-intermediate (<1 μs). For GPR, photocycles between 100 and 200 ms have been reported (3,32,52,65,66). The longer photocycle for GPR_{A178R} is caused by the elongated lifetime of the N/O intermediate and the interconversion of two different N intermediates. The decay of these intermediates is correlated with the reprotoonation of the primary proton donor. In BR at pH > 9, a reaction scheme $M_1 \rightarrow M_2 \rightarrow N_1 \rightarrow N_2 \rightarrow BR$ was found, where N_1 and N_2 are referred to as the N intermediates before and after reprotoonation of D96 (67,68). In GPR, the primary proton donor E108 is found in helix C, in which a number of mutation-induced chemical shift changes were observed (Figs. 7 and 8). It has been observed in BR that this step of proton uptake involves an outward motion of helix F facilitating the proton uptake from the cytoplasmic side, most probably due to the entrance of water molecules (69–72). After proton uptake from the cytoplasmic surface this outward movement of the F-helix is reversed (73). Assuming a similar mechanism in GPR leads to the conclusion that the restoring force imposed by the structured EF loop to helices E and F is significantly reduced in GPR_{A178R} resulting in slower helix reorientation, hence an elongated lifetime of the N/O intermediate. Therefore, the native EF loop seems to play a major role in proton uptake from the cytoplasmic side of GPR. This conclusion is also supported by a combined EPR and DNP study in which altered hydration levels upon illumination indicated an EF loop movement (46). However, the capability of proton pumping is not affected by this mutation as shown by light-induced pH changes in spheroblast vesicles (15) and by black lipid membrane experiments (Fig. S9).

CONCLUSION

We have shown by time-resolved optical spectroscopy that the EF-loop mutation A178R in GPR does not only cause a redshift but slows down the primary reaction, weakens its pH dependence, and slows down the complete photocycle due to the elongated lifetime of the N/O intermediates. Using conventional and DNP-enhanced solid-state NMR, we have identified the molecular origin of these surprising effects. Introducing a bulky residue such as R at position 178 disrupts the secondary EF-loop structure. The resulting

distorted loop structure imposes weaker structural constraints on E and F helices compared to GPR, which alters the structure of the retinal binding site. As a consequence, the chromophore color, the primary reaction as well as late stages of the photocycle, involving E and F helix movements during proton uptake, are affected. Our data indicate that the EF loop plays an important role for proton uptake similar to BR (69). On the other hand, our data also show that an interaction pathway exists between the EF loop and retinal binding pocket. One could speculate that in this way signals could be transmitted across the membrane needed for potentially additional functions of GPR such as sensing or signaling. Our study also illustrates that advanced methodology such as DNP/solid-state NMR and time-resolved optical spectroscopy provides highly compatible data sets if properly combined and enables obtaining unprecedented insight into the molecular mechanism of retinal proteins. A related study on mechanism of the major green/blue switch L105Q in GPR will be reported elsewhere.

SUPPORTING MATERIAL

Nine figures, two tables, and references (74–79) are available at [http://www.biophysj.org/biophysj/supplemental/S0006-3495\(13\)00692-9](http://www.biophysj.org/biophysj/supplemental/S0006-3495(13)00692-9).

Lenica Reggie, Vasyl Denysenkov, Jörn Plackmeyer, and Thomas Prisner, BMRZ Frankfurt are acknowledged for their support with our DNP setup. We are grateful to Daniel Gottstein and Peter Güntert, BMRZ Frankfurt, for helpful discussions and GPR structure modeling. Marie Concistre and Malcolm H. Levitt, Southampton are acknowledged for helpful advice on the HCCH data analysis. We thank Anja Becker, MPI Biophysics, Frankfurt, for help with BLM experiments.

This work was funded by SFB 807 Transport and communication across membranes. The DNP experiments were enabled through an equipment grant provided by the Deutsche Forschungsgemeinschaft (DFG) (Cluster of Excellence Macromolecular Complexes Frankfurt).

REFERENCES

- Bamann, C., T. Kirsch, ..., E. Bamberg. 2008. Spectral characteristics of the photocycle of channelrhodopsin-2 and its implication for channel function. *J. Mol. Biol.* 375:686–694.
- Takahashi, T., B. Yan, ..., J. L. Spudich. 1990. Color regulation in the archaeabacterial phototaxis receptor phoborhodopsin (sensory rhodopsin II). *Biochemistry*. 29:8467–8474.
- Friedrich, T., S. Geibel, ..., E. Bamberg. 2002. Proteorhodopsin is a light-driven proton pump with variable vectoriality. *J. Mol. Biol.* 321:821–838.
- Oesterhelt, D., and W. Stoeckenius. 1971. Rhodopsin-like protein from the purple membrane of *Halobacterium halobium*. *Nat. New Biol.* 233:149–152.
- Béjà, O., E. N. Spudich, ..., E. F. DeLong. 2001. Proteorhodopsin phototrophy in the ocean. *Nature*. 411:786–789.
- Man, D., W. Wang, ..., O. Béjà. 2003. Diversification and spectral tuning in marine proteorhodopsins. *EMBO J.* 22:1725–1731.
- Grossjean, M. F., and P. Tavan. 1988. Wavelength regulation in bacteriorhodopsin and halorhodopsin - a Pariser-Parr-Pople multireference double excitation configuration-interaction study of retinal dyes. *J. Chem. Phys.* 88:4884–4896.
- Sekharan, S., M. Sugihara, and V. Buss. 2007. Origin of spectral tuning in rhodopsin—it is not the binding pocket. *Angew. Chem. Int. Ed. Engl.* 46:269–271.
- Kochendoerfer, G. G., S. W. Lin, ..., R. A. Mathies. 1999. How color visual pigments are tuned. *Trends Biochem. Sci.* 24:300–305.
- Hoffmann, M., M. Wanko, ..., M. Elstner. 2006. Color tuning in rhodopsins: the mechanism for the spectral shift between bacteriorhodopsin and sensory rhodopsin II. *J. Am. Chem. Soc.* 128:10808–10818.
- Wanko, M., M. Hoffmann, ..., M. Elstner. 2005. Calculating absorption shifts for retinal proteins: computational challenges. *J. Phys. Chem. B.* 109:3606–3615.
- Yan, B., J. L. Spudich, ..., K. Nakanishi. 1995. Spectral tuning in bacteriorhodopsin in the absence of counterion and coplanarization effects. *J. Biol. Chem.* 270:29668–29670.
- Wang, W. W., O. A. Sineshchekov, ..., J. L. Spudich. 2003. Spectroscopic and photochemical characterization of a deep ocean proteorhodopsin. *J. Biol. Chem.* 278:33985–33991.
- Yoshitsugu, M., M. Shibata, ..., H. Kandori. 2008. Color change of proteorhodopsin by a single amino acid replacement at a distant cytoplasmic loop. *Angew. Chem. Int. Ed. Engl.* 47:3923–3926.
- Yoshitsugu, M., J. Yamada, and H. Kandori. 2009. Color-changing mutation in the E-F loop of proteorhodopsin. *Biochemistry*. 48:4324–4330.
- Otomo, J. 1996. Influence exercised by histidine-95 on chloride transport and the photocycle in halorhodopsin. *Biochemistry*. 35:6684–6689.
- Yamada, K., A. Kawanabe, and H. Kandori. 2010. Importance of alanine at position 178 in proteorhodopsin for absorption of prevalent ambient light in the marine environment. *Biochemistry*. 49:2416–2423.
- Fuhrman, J. A., M. S. Schwalbach, and U. Stigl. 2008. Proteorhodopsins: an array of physiological roles? *Nat. Rev. Microbiol.* 6:488–494.
- Hempelmann, F., S. Höpfer, ..., C. Glaubitz. 2011. His75-Asp97 cluster in green proteorhodopsin. *J. Am. Chem. Soc.* 133:4645–4654.
- Bergo, V. B., O. A. Sineshchekov, ..., J. L. Spudich. 2009. His-75 in Proteorhodopsin, a Novel Component in Light-driven Proton Translocation by Primary Pumps. *J. Biol. Chem.* 284:2836–2843.
- Klyszejko, A. L., S. Shastri, ..., C. Glaubitz. 2008. Folding and assembly of proteorhodopsin. *J. Mol. Biol.* 376:35–41.
- Hoffmann, J., L. Aslimovska, ..., B. Brutschy. 2010. Studying the stoichiometries of membrane proteins by mass spectrometry: microbial rhodopsins and a potassium ion channel. *Phys. Chem. Chem. Phys.* 12:3480–3485.
- Shi, L., M. A. Ahmed, ..., V. Ladizhansky. 2009. Three-dimensional solid-state NMR study of a seven-helical integral membrane proton pump—structural insights. *J. Mol. Biol.* 386:1078–1093.
- Shi, L. C., E. M. R. Lake, ..., V. Ladizhansky. 2009. Solid-state NMR study of proteorhodopsin in the lipid environment: secondary structure and dynamics. *Biochim. Biophys. Acta*. 1788:2563–2574.
- Yang, J., L. Aslimovska, and C. Glaubitz. 2011. Molecular dynamics of proteorhodopsin in lipid bilayers by solid-state NMR. *J. Am. Chem. Soc.* 133:4874–4881.
- Pfleger, N., M. Lorch, ..., C. Glaubitz. 2008. Characterisation of Schiff base and chromophore in green proteorhodopsin by solid-state NMR. *J. Biomol. NMR.* 40:15–21.
- Reckel, S., D. Gottstein, ..., V. Dötsch. 2011. Solution NMR structure of proteorhodopsin. *Angew. Chem. Int. Ed. Engl.* 50:11942–11946.
- Stehle, J., F. Scholz, ..., H. Schwalbe. 2012. Characterization of the ground state dynamics of proteorhodopsin by NMR and optical spectroscopies. *J. Biomol. NMR.* 54:401–413.
- Maly, T., G. T. Debelouchina, ..., R. G. Griffin. 2008. Dynamic nuclear polarization at high magnetic fields. *J. Chem. Phys.* 128:052211–052219.

30. Pardoen, J., C. Winkel, ..., J. Lugtenburg. 1984. Synthesis of retinals labeled at positions 14 and 15 (with C-13 and or H-2). *Recl. Trav. Chim. Pays-Bas.* 103:135–141.
31. Song, C. S., K. N. Hu, ..., R. G. Griffin. 2006. TOTAPOL: a biradical polarizing agent for dynamic nuclear polarization experiments in aqueous media. *J. Am. Chem. Soc.* 128:11385–11390.
32. Váró, G., L. S. Brown, ..., J. K. Lanyi. 2003. Characterization of the photochemical reaction cycle of proteorhodopsin. *Biophys. J.* 84:1202–1207.
33. Hohwy, M., H. J. Jakobsen, ..., N. C. Nielsen. 1998. Broadband dipolar recoupling in the nuclear magnetic resonance of rotating solids: a compensated C7 pulse sequence. *J. Chem. Phys.* 108:2686–2694.
34. Fung, B. M., A. K. Khitrin, and K. Ermolaev. 2000. An improved broadband decoupling sequence for liquid crystals and solids. *J. Magn. Reson.* 142:97–101.
35. Concistrè, M., O. G. Johannessen, ..., M. H. Levitt. 2012. A large geometric distortion in the first photointermediate of rhodopsin, determined by double-quantum solid-state NMR. *J. Biomol. NMR.* 53:247–256.
36. Vinogradov, E., P. K. Madhu, and S. Vega. 1999. High-resolution proton solid-state NMR spectroscopy by phase-modulated Lee-Goldburg experiment. *Chem. Phys. Lett.* 314:443–450.
37. Bak, M., J. T. Rasmussen, and N. C. Nielsen. 2000. SIMPSON: a general simulation program for solid-state NMR spectroscopy. *J. Magn. Reson.* 147:296–330.
38. Sharaabi, Y., V. Brumfeld, and M. Sheves. 2010. Binding of anions to proteorhodopsin affects the Asp97 pK(a). *Biochemistry.* 49:4457–4465.
39. Hu, J., R. G. Griffin, and J. Herzenfeld. 1994. Synergy in the spectral tuning of retinal pigments: complete accounting of the opsin shift in bacteriorhodopsin. *Proc. Natl. Acad. Sci. USA.* 91:8880–8884.
40. Carravetta, M., X. Zhao, ..., M. H. Levitt. 2004. Protein-induced bonding perturbation of the rhodopsin chromophore detected by double-quantum solid-state NMR. *J. Am. Chem. Soc.* 126:3948–3953.
41. Song, L., M. A. El-Sayed, and J. K. Lanyi. 1996. Effect of changing the position and orientation of Asp85 relative to the protonated Schiff base within the retinal cavity on the rate of photoisomerization in bacteriorhodopsin. *J. Phys. Chem.* 100:10479–10481.
42. Song, L., M. A. El-Sayed, and J. K. Lanyi. 1993. Protein catalysis of the retinal subpicosecond photoisomerization in the primary process of bacteriorhodopsin photosynthesis. *Science.* 261:891–894.
43. Logunov, S. L., M. A. El-Sayed, ..., J. K. Lanyi. 1996. Photoisomerization quantum yield and apparent energy content of the K intermediate in the photocycles of bacteriorhodopsin, its mutants D85N, R82Q, and D212N, and deionized blue bacteriorhodopsin. *J. Phys. Chem.* 100:2391–2398.
44. Huber, R., T. Köhler, ..., J. Wachtveitl. 2005. pH-dependent photoisomerization of retinal in proteorhodopsin. *Biochemistry.* 44:1800–1806.
45. Lenz, M. O., R. Huber, ..., J. Wachtveitl. 2006. First steps of retinal photoisomerization in proteorhodopsin. *Biophys. J.* 91:255–262.
46. Hussain, S., J. M. Franck, and S. Han. 2013. Transmembrane protein activation refined by site-specific hydration dynamics. *Angew. Chem. Int. Ed. Engl.* 52:1953–1958.
47. Alexiev, U., I. Rimke, and T. Pöhlmann. 2003. Elucidation of the nature of the conformational changes of the EF-interhelical loop in bacteriorhodopsin and of the helix VIII on the cytoplasmic surface of bovine rhodopsin: a time-resolved fluorescence depolarization study. *J. Mol. Biol.* 328:705–719.
48. Higman, V. A., K. Varga, ..., A. Watts. 2011. The conformation of bacteriorhodopsin loops in purple membranes resolved by solid-state MAS NMR spectroscopy. *Angew. Chem. Int. Ed. Engl.* 50:8432–8435.
49. Schubert, M., M. Kolbe, ..., P. Schmieder. 2002. Heteronuclear multidimensional NMR spectroscopy of solubilized membrane proteins: resonance assignment of native bacteriorhodopsin. *ChemBioChem.* 3:1019–1023.
50. Ulfers, A. L., J. L. McMurry, ..., D. F. Mierke. 2002. Structure of the third intracellular loop of the human cannabinoid 1 receptor. *Biochemistry.* 41:11344–11350.
51. Yeagle, P. L., J. L. Alderfer, and A. D. Albert. 1995. Structure of the third cytoplasmic loop of bovine rhodopsin. *Biochemistry.* 34:14621–14625.
52. Lakatos, M., J. K. Lanyi, ..., G. Váró. 2003. The photochemical reaction cycle of proteorhodopsin at low pH. *Biophys. J.* 84:3252–3256.
53. Ikeda, D., Y. Furutani, and H. Kandori. 2007. FTIR study of the retinal Schiff base and internal water molecules of proteorhodopsin. *Biochemistry.* 46:5365–5373.
54. Blatz, P. E., J. H. Mohler, and H. V. Navangul. 1972. Anion-induced wavelength regulation of absorption maxima of Schiff bases of retinal. *Biochemistry.* 11:848–855.
55. Hufen, J., M. Sugihara, and V. Buss. 2004. How the counterion affects ground- and excited-state properties of the rhodopsin chromophore. *J. Phys. Chem. B.* 108:20419–20426.
56. Schenkl, S., F. van Mourik, ..., M. Chergui. 2005. Probing the ultrafast charge translocation of photoexcited retinal in bacteriorhodopsin. *Science.* 309:917–920.
57. Garavelli, M., P. Celani, ..., M. Olivucci. 1997. The $C_5H_6NH_2^+$ protonated Schiff base: an ab initio minimal model for retinal photoisomerization. *J. Am. Chem. Soc.* 119:6891–6901.
58. Mathies, R., and L. Stryer. 1976. Retinal has a highly dipolar vertically excited singlet state: implications for vision. *Proc. Natl. Acad. Sci. USA.* 73:2169–2173.
59. González-Luque, R., M. Garavelli, ..., M. Olivucci. 2000. Computational evidence in favor of a two-state, two-mode model of the retinal chromophore photoisomerization. *Proc. Natl. Acad. Sci. USA.* 97:9379–9384.
60. Logunov, S. L., M. A. El-Sayed, and J. K. Lanyi. 1996. Catalysis of the retinal subpicosecond photoisomerization process in acid purple bacteriorhodopsin and some bacteriorhodopsin mutants by chloride ions. *Biophys. J.* 71:1545–1553.
61. Scholz, F., E. Bamberg, ..., J. Wachtveitl. 2012. Tuning the primary reaction of channelrhodopsin-2 by imidazole, pH, and site-specific mutations. *Biophys. J.* 102:2649–2657.
62. Cembran, A., F. Bernardi, ..., M. Garavelli. 2004. Counterion controlled photoisomerization of retinal chromophore models: a computational investigation. *J. Am. Chem. Soc.* 126:16018–16037.
63. Imashева, E. S., K. Shimono, ..., J. K. Lanyi. 2005. Formation of a long-lived photoproduct with a deprotonated Schiff base in proteorhodopsin, and its enhancement by mutation of Asp227. *Biochemistry.* 44:10828–10838.
64. Herz, J., M. K. Verhoeven, ..., J. Wachtveitl. 2012. Critical role of Asp227 in the photocycle of proteorhodopsin. *Biochemistry.* 51:5589–5600.
65. Ranaghan, M. J., C. T. Schwall, ..., R. R. Birge. 2011. Green proteorhodopsin reconstituted into nanoscale phospholipid bilayers (nanodiscs) as photoactive monomers. *J. Am. Chem. Soc.* 133:18318–18327.
66. Dioumaev, A. K., L. S. Brown, ..., J. K. Lanyi. 2002. Proton transfers in the photochemical reaction cycle of proteorhodopsin. *Biochemistry.* 41:5348–5358.
67. Váró, G., R. Needleman, and J. K. Lanyi. 1996. Protein structural change at the cytoplasmic surface as the cause of cooperativity in the bacteriorhodopsin photocycle. *Biophys. J.* 70:461–467.
68. Zimányi, L., Y. Cao, ..., J. K. Lanyi. 1993. Pathway of proton uptake in the bacteriorhodopsin photocycle. *Biochemistry.* 32:7669–7678.
69. Subramanian, S., and R. Henderson. 2000. Molecular mechanism of vectorial proton translocation by bacteriorhodopsin. *Nature.* 406:653–657.
70. Lanyi, J. K., and H. Luecke. 2001. Bacteriorhodopsin. *Curr. Opin. Struct. Biol.* 11:415–419.
71. Hirai, T., and S. Subramanian. 2009. Protein conformational changes in the bacteriorhodopsin photocycle: comparison of findings from electron and X-ray crystallographic analyses. *PLoS ONE.* 4:e5769.

72. Vonck, J. 2000. Structure of the bacteriorhodopsin mutant F219L N intermediate revealed by electron crystallography. *EMBO J.* 19:2152–2160.
73. Thorgeirsson, T. E., W. Z. Xiao, ..., Y. K. Shin. 1997. Transient channel-opening in bacteriorhodopsin: an EPR study. *J. Mol. Biol.* 273:951–957.
74. Bergen, H., H. Furr, and J. Olson. 1988. Synthesis of tri-deuterated tetra-deuterated and penta-deuterated forms of Vitamin-A. *J. Labelled Comp. Radiopharm.* 25:11–21.
75. Magoulas, G. E., S. E. Bariamis, ..., G. Maroulis. 2011. Syntheses, antiproliferative activity and theoretical characterization of acitretin-type retinoids with changes in the lipophilic part. *Eur. J. Med. Chem.* 46:721–737.
76. McLean, N., A. Gansmuller, ..., R. Brown. 2011. Syntheses of C-13(2)-labelled 11Z-retinals. *Tetrahedron.* 67:8404–8410.
77. Sadhukhan, S., Y. Han, ..., G. P. Tochrop. 2010. Using isotopic tools to dissect and quantitate parallel metabolic pathways. *J. Am. Chem. Soc.* 132:6309–6311.
78. Tanumihardjo, S. 2001. Synthesis of 10,11,14,15-C-13(4)- and 14,15-C-13(2)-retinyl acetate. *J. Labelled Comp. Radiopharm.* 44:365–372.
79. Wada, A., Y. Ieki, ..., M. Ito. 2005. Palladium-catalyzed coupling reaction of an enol nonaflate with (vinyl)tributylstannanes and acetylenes: a highly stereoselective synthesis of 8,18-C-13(2)-labeled retinal. *Synthesis.* 1581–1588.

SUPPORTING INFORMATION

The EF Loop in Green Proteorhodopsin affects Conformation and Photocycle dynamics

Michaela Mehler^{*1}, Frank Scholz^{*2}, Sandra J. Ullrich¹, Jiafei Mao¹, Markus Braun², Lynda J. Brown³, Richard C. D. Brown³, Sarah A. Fiedler¹, Johanna Becker-Baldus¹, Josef Wachtveitl^{**2} & Clemens Glaubitz^{*1}

(1) Institute of Biophysical Chemistry & Centre for Biomolecular Magnetic Resonance, Goethe-University Frankfurt, Germany

(2) Institute of Physical and Theoretical Chemistry, Goethe-University Frankfurt, Germany

(3) Department of Chemistry, University of Southampton

(*) Contributed equally.

(**) Corresponding authors: glaubitz@em.uni-frankfurt.de, wveitl@theochem.uni-frankfurt.de.

1. Sample Preparation

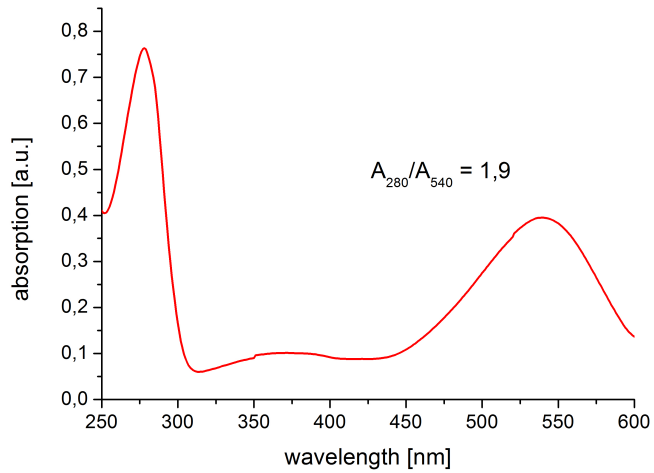


Fig. S1: Absorption spectrum of GPR_{A178R} solubilized in 0.05 % DDM at pH 7.5 reveals high sample purity.

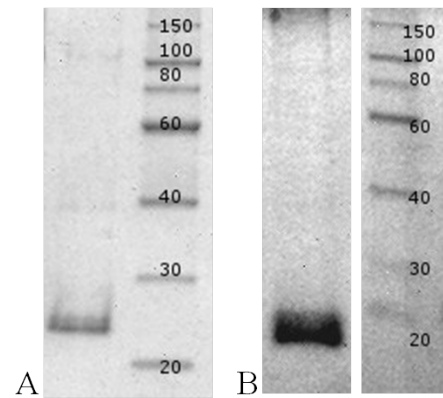
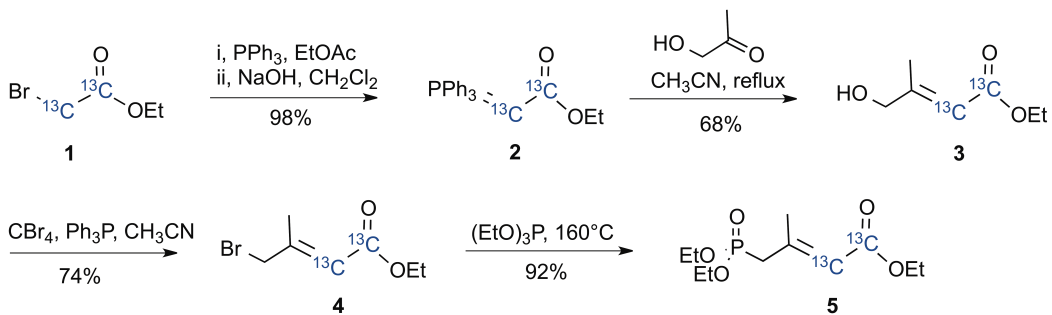


Fig. S2: SDS-PAGE of GPR (A) and GPR_{A178R} (B) in DMPC/DMPA liposomes.

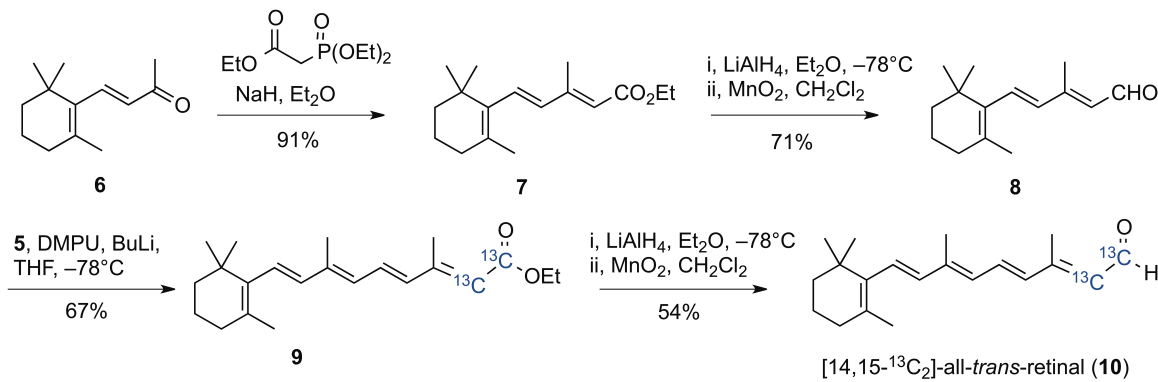
2. Synthesis of [14,15-¹³C₂]-all-trans-Retinal

[14,15-¹³C₂]-all-trans-retinal has been synthesized previously (1), although a modified route was adopted in this work. The synthesis is summarized in schemes 1 and 2, starting from ethyl [¹³C]-bromoacetate (99 atom % ¹³C, Sigma-Aldrich) and β-ionone. Thus, ethyl [¹³C₂]-bromoacetate was converted to the known labeled phosphonium ylide **2** (2), which underwent an *E*-selective olefination with hydroxyacetone to afford allylic alcohol **3** (3). The alcohol **3** was converted to the bromide **4** followed by Arbusov reaction with triethylphosphite to provide the doubly ¹³C-labeled phosphonate **5** (3).



Scheme 1. Synthesis of [1,2-¹³C₂]-(*E*)-ethyl 4-(diethoxyphosphoryl)-3-methylbut-2-enoate

The all-*trans* trienal **8** was obtained by Horner-Wadsworth-Emmons reaction between β-ionone and triethyl phosphonoacetate followed by ester reduction and alcohol oxidation (4-6). The aldehyde **8** is rather sensitive towards isomerization and care should be taken during purification and storage (4). [14,15-¹³C₂]-all-*trans*-ethyl retinoate (**9**) was obtained from reaction of lithiated derivative of phosphonate fragment **5** with aldehyde **8** (7). The ester functionality was reduced to the allylic alcohol using LiAlH₄, followed by oxidation using MnO₂ to deliver the required [14,15-¹³C₂]-all-*trans*-retinal (**10**) (7). Spectroscopic and physical data for [14,15-¹³C₂]-all-*trans*-retinal were consistent with the reported data (1).



Scheme 2. Synthesis of [14,15-¹³C₂]-all-*trans*-retinal

3. Supporting Solid-State NMR Data

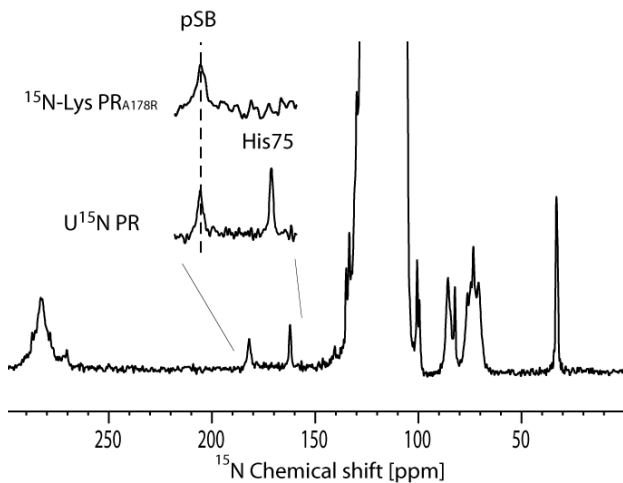


Fig. S3: ¹⁵N-CP-MAS spectra of U-¹⁵N-GPR and ¹⁵N-Lys-GPR_{A178R} in DMPC/DMPA liposomes at pH 9. The pSB chemical shift in both cases is similar (GPR_{A178}: 182.1 ppm, GPR: 182.0 ppm). The signals of the pSB or of the side chains of His75 could not unambiguously be identified in U-¹⁵N-GPR_{A178R} due to signal overlap with resonances from the His-tag (not shown). Spectra were recorded on a 600 MHz spectrometer equipped with a 4mm MAS probe head at 270 K and 10 kHz MAS sample rotation rate. For GPR_{A178R} approx. 10 mg protein and 21k scans and for GPR approx. 18 mg protein and 10k scans were used.

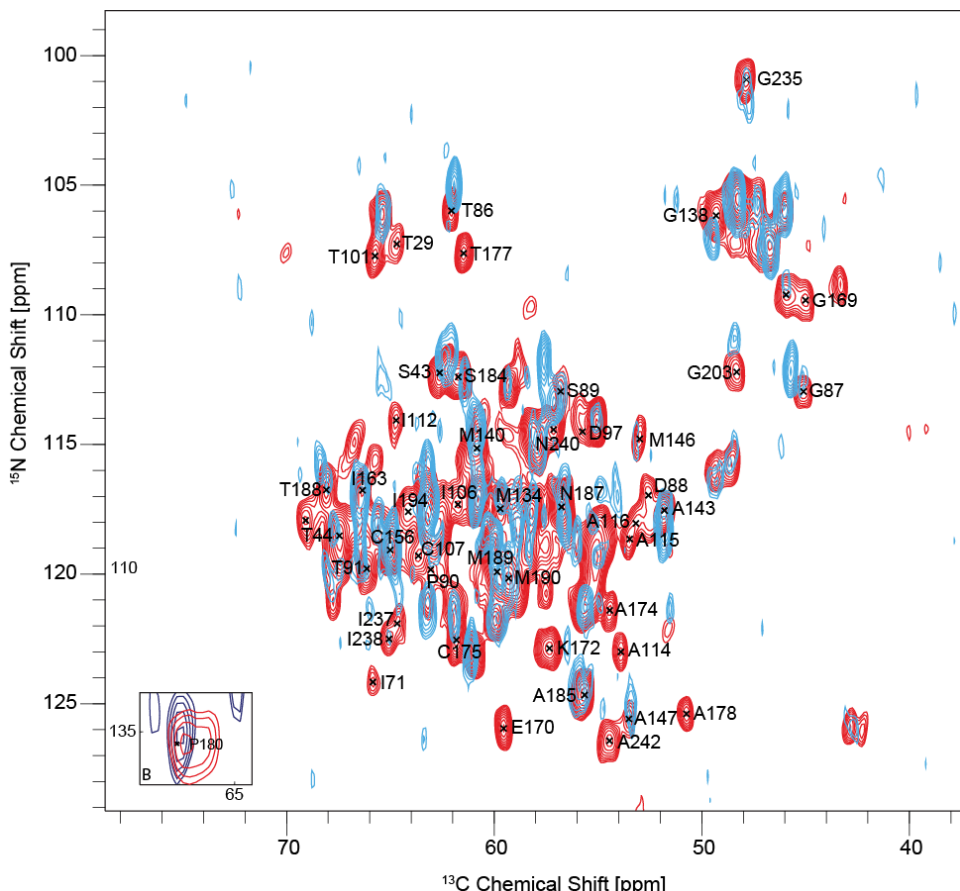


Fig. S4: Comparison of NCA spectra of GPR_{A178R} (blue) with GPR (red). Resonances were assigned using NCACX and NCOCX experiments and were compared to those reported for GPR (8). A summary is given in Tab. S1.

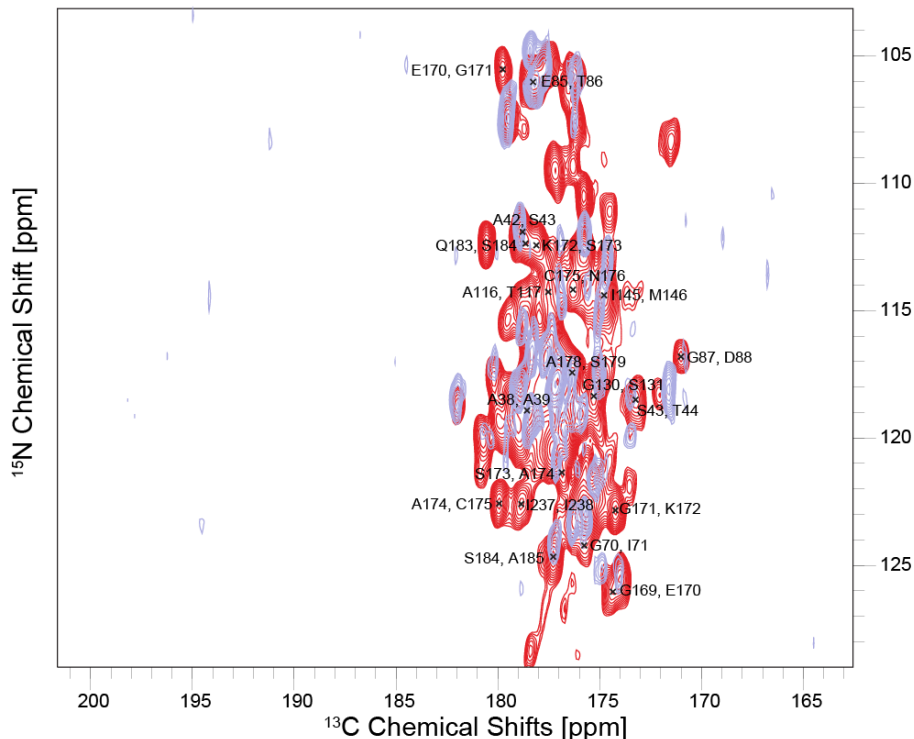


Fig. S5: Comparison of NCO spectra of GPR_{A178R} (blue) with GPR (red). Resonances were assigned using NCACX and NCOCX experiments and were compared to those reported for GPR (8). A summary is given in Tab. S1.

Tab. S1: Overview of residues affected by the A178R mutation

Only those resonances are listed for which a chemical shift change >0.2 ppm in GPR_{A178R} compared to GPR has been observed.

		WT	A178R		
Residue	Atom	Shift [ppm]	Shift [ppm]	Shift difference [ppm]	
29Thr	N Cb	106,93 69,41	107,28 69,19	-0,35 0,23	NCA, Fig. S4 PDSD, Ca-Cb (Fig. 3E), Cg2-Cb (Fig. 3G)
38Ala	C	178,42	178,80	-0,38	NCO, 38-Ala/39-Ala
39Ala	N	118,79	118,33	0,46	NCO, 38-Ala/39-Ala
43Ser	C N Ca	173,13 111,95 62,43	173,45 111,40 62,10	-0,31 0,55 0,33	NCO, 43-Ser/44-Thr / Fig. S5 NCO, 42-Ala/43-Ser / Fig. S5 NCA, Fig. S4
44Thr	N Ca Cg2	118,39 67,36 21,07	118,73 67,59 20,66	-0,35 -0,24 0,41	NCO, 43-Ser/44-Thr / Fig. S5 NCA, Fig. S4 PDSD, Cg2-Cb (Fig. 3G)
71Ile	N Ca	124,18 65,72	125,13 65,97	-0,95 -0,25	NCO, 70-Gly/71-Ile / Fig. S5 NCA, Fig. S4
85Glu	C	178,21	177,61	0,60	NCO, 85-Glu/86-Thr / Fig. S5

86Thr	N Ca Cg2	105,81 61,97 21,02	104,43 61,73 21,41	1,38 0,25 -0,39	NCO, 85-Glu/86-Thr / Fig. S5 NCA, Fig. S4, PDSD Ca-Cb (Fig.3E), Cg2-Ca (Fig.3G)
87Gly	Ca	44,83	44,50	0,32	NCA, Fig. S4
88Asp	N	116,75	not assigned		NCO, 87-Gly/88-Asp / Fig. S5
89Ser	N Ca	112,76 56,68	113,09 56,98	-0,32 -0,30	NCA, Fig. S4 PDSD, Ca-Cb (Fig. 3E)
90Pro	Ca Cb	63,12 32,43	62,82 32,12	0,29 0,31	PDSD, Cb-Ca (Fig. 3C) PDSD, Cb-Ca (Fig. 3C)
91Thr	N	119,60	121,21	-1,62	NCA, Fig. S4
97Asp	Cb	42,27	41,56	0,71	PDSD, Cb-Ca (Fig. 3B)
101Thr	Ca Cb Cg2	65,56 69,59 23,12	65,86 69,33 22,81	-0,30 0,26 0,31	PDSD Ca-Cb (Fig. 3E), NCA, Fig. S4 PDSD, Cg2-Cb (Fig. 3G) PDSD, Cg2-Cb (Fig. 3G)
103Pro	Ca Cd	65,18 50,67	65,56 50,11	-0,38 0,56	PDSD, Cd-Ca (Fig. 3F) PDSD, Cd-Ca (Fig. 3F)
106Ile	N Ca Cb	117,18 61,60 39,33	116,47 60,89 39,71	0,71 0,71 -0,38	NCA, Fig. S4 PDSD, Cb-Ca(Fig. 3C) PDSD, Cb-Ca (Fig. 3C)
107Cys	N Ca	119,28 63,73	120,02 63,50	-0,74 0,23	NCA, Fig. S4 NCA, Fig. S4, PDSD Cb-Ca (Fig. 3G)
112Ile	Ca Cg2	64,58 18,29	not assigned not assigned		PDSD, Cg2-Ca (Fig. 3G) PDSD, Cg2-Ca(Fig. 3G)
114Ala	N	122,85	122,38	0,47	NCA, Fig. S4
115Ala	Ca Cb	53,28 15,61	not assigned not assigned		PDSD, Cb-Ca (Fig. 3D) PDSD, Cb-Ca(Fig. 3D)
116Ala	N Ca Cb	118,18 52,86 23,81	118,80 not assigned not assigned	-0,62	NCA, Fig. S4 PDSD, Cb-Ca (Fig. 3D) PDSD, Cb-Ca (Fig. 3D)
117Thr	N	114,78	115,48	-0,69	NCO,116-Ala/117-Thr / Fig. S5
126Lys	Cb Cd Ce	34,42 30,24 42,74	34,03 29,86 42,47	0,39 0,37 0,27	PDSD, Cb-Ca, (Fig. 3C) PDSD, Cd-Ce (Fig. 3A) PDSD Cg-Ce (Fig. 3A)
131Ser	N	118,03	117,50	0,53	NCO, 130-Gly/131-Ser / Fig. S5
134Met	N Cb Cg	117,46 34,82 30,16	118,51 35,31 29,91	-1,04 -0,50 0,26	NCA, Fig. S4 PDSD, Cb-Ca (Fig. 3C) PDSD, Cg-Cb (Fig. 3A)
138Gly	N	105,98	106,35	-0,37	NCA, Fig. S4
140Met	N	115,11	114,43	0,67	NCA, Fig. S4
143Ala	N	117,54	117,87	-0,33	NCA, Fig. S4
145Ile	C Cb Cg1	174,71 39,29 29,04	174,99 39,09 28,73	-0,28 0,20 0,32	NCO, 145-Ile/146-Met / Fig. S5 PDSD, Cb-Ca (Fig. 3C) Cg1-Ca (Fig. 3G)
146Met	N	114,40	115,07	-0,67	NCO, 145-Ile/146-Met / Fig. S5
147Ala	N Ca	125,74 53,36	125,04 53,14	0,69 0,23	NCA, Fig. S4 NCA, Fig. S4
156Cys	N	118,95	118,59	0,36	NCA, Fig. S4
163Ile	N	116,75	117,11	-0,35	NCA, Fig. S4
168Ala	Cb	22,67	22,36	0,31	PDSD Cb-Ca (Fig. 3D)
169Gly	C	174,24	173,95	0,30	NCO, 169-Gly/170-Glu / Fig. S5

170Glu	C N Ca	179,62 125,88 59,35	179,37 125,21 not assigned	0,25 0,67	NCO, 170-Glu/171-Gly / Fig. S5 NCO, 169-Gly/170-Glu / Fig. S5 NCA, Fig. S4
171Gly	C	174,15	174,37	-0,22	NCO, 171-Gly/172-Lys / Fig. S5
172Lys	C N Cg Cd	178,01 122,76 23,49 27,72	177,72 123,82 22,38 27,03	0,28 -1,06 1,12 0,69	NCO, 172-Lys/173-Ser / Fig. S5 NCA, Fig. S4 PDSD, Cg-Cd (Fig. 3A) PDSD, Cd-Ca (Fig. 3C)
173Ser	C	176,72	177,10	-0,39	NCO, 173-Ser/174-Ala / Fig. S5
174Ala	C N Ca	179,77 121,22 54,29	180,30 120,64 53,81	-0,53 0,58 0,48	NCO, 174-Ala/175-Cys / Fig. S5 NCA, Fig. S4 PDSD, Cb-Ca (Fig. 3D)
175Cys	C N Ca	176,22 122,48 61,65	176,98 120,41 61,03	-0,76 2,07 0,61	NCO, 175-Cys/176-Asn / Fig. S5 NCA, Fig. S4 PDSD, Cb-Ca (Fig. 3G)
176Asn	Cb	38,26	39,04	-0,78	PDSD, Cb-Ca (Fig. 3B)
177Thr	Ca Cb	61,34 70,06	60,94 68,98	0,39 1,08	PDSD, Ca-Cb (Fig. 3E) PDSD, Ca-Cb, Cg2-Cb (Fig. 3E/G)
180Pro	N Ca Cb Cg	135,13 65,88 31,74 28,00	134,78 66,21 31,26 28,32	0,35 -0,33 0,48 -0,32	NCA, Fig. S4 PDSD, Cb-Ca (Fig. 3C), Cg-Ca (Fig. 3B), Cd-Ca (Fig. 3F) PDSD, Cb-Ca (Fig. 3C) PDSD, Cg-Ca (Fig. 3C)
183Gln	C	178,55	178,24	0,31	NCO, 183-Gln/184-Ser / Fig. S5
184Ser	Ca	61,51	61,23	0,28	NCA, Fig. S4
185Ala	N Ca	124,55 55,44	123,86 55,20	0,69 0,25	NCA, Fig. S4 NCA, Fig. S4, PDSD Cb-Ca (Fig. 3D)
187Asn	N Ca Cb	117,20 56,56 38,26	116,61 56,31 38,05	0,59 0,25 0,21	NCA, Fig. S4 PDSD, Cb-Ca (Fig. 3C) PDSD, Cb-Ca (Fig. 3C)
188Thr	N	116,64	115,63	1,00	NCA, Fig. S4
189Met	Ca Cb	59,93 35,90	60,44 36,22	-0,50 -0,32	PDSD, Cb-Ca (Fig. 3C) PDSD, Cb-Ca (Fig. 3C)
190Met	Ca	59,12	59,67	-0,55	NCA, Fig. S4
194Ile	Cb	39,69	39,22	0,47	PDSD, Cg1-Cb, Cg2-Cb (Fig. 3A) Cb-Ca (Fig. 3C)
201Pro	Cg	27,30	26,99	0,31	PDSD, Cg-Ca (Fig. 3B)
203Gly	N	111,93	110,68	1,25	NCA, Fig. S4
206Thr	N	105,09	104,49	0,60	NCACX
224Asn	Cb	36,37	36,10	0,27	PDSD, Cb-Ca (Fig. 3B)
227Asp	N Ca	119,04 58,12	118,11 57,73	0,93 0,39	PDSD, Cb-Ca (Fig. 3C) PDSD, Cb-Ca (Fig. 3C)
232Ile	Cb Cg2	37,01 16,20	36,77 15,99	0,24 0,20	PDSD, Cb-Ca (Fig. 3C) PDSD, Cg2-Ca (Fig. 3G)
235Gly	N	100,61	101,43	-0,82	NCA, Fig. S4
238Ile	N	122,46	122,77	-0,31	NCO, Ile-237/Ile-238 / Fig. S5
240Asn	Cb	40,07	39,76	0,31	PDSD, Cb-Ca (Fig. 3C)
242Ala	N	126,48	125,78	0,70	NCA, Fig. S4

4. Optical Spectroscopy: Data Analysis and Supporting Information

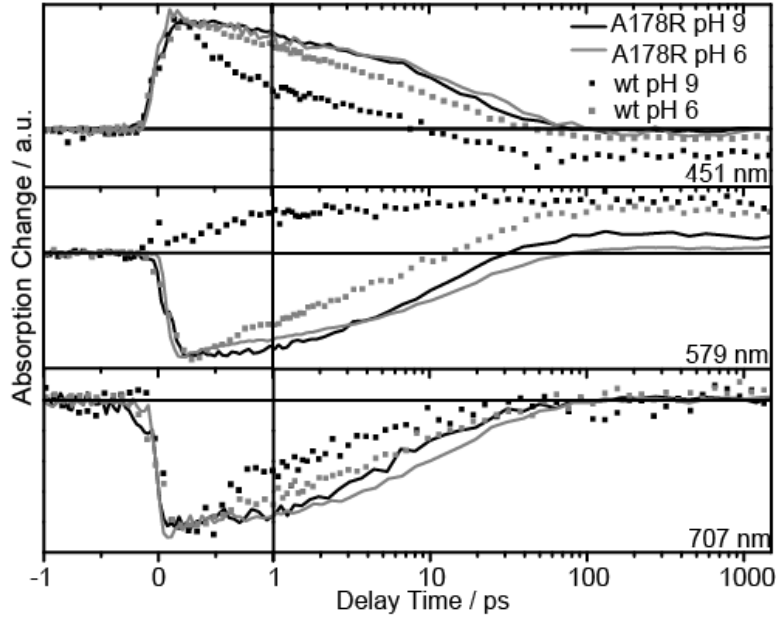


Fig. S6: Comparison of the absorption changes at 451 nm (decay of the excited state, ESA), 579 nm (ground state bleach/photoproduct formation, GSB) and 707 nm (stimulated emission, SE) taken from Fig. 4. Both signals for ESA and SE evolve and decay on the same time-scale since both reflect the lifetime of the excited state. As can be seen, the lifetime of the excited state in GPR is dramatically shortened at pH 9 compared to pH 6, which is much less the case for GPR_{A178R}. The transient absorbance signal monitored at 579 nm is mainly caused by the decay of the GSB at early delay times and the photoproduct formation at longer delay times. No GSB decay at early delay times is observed for GPR at pH 9.

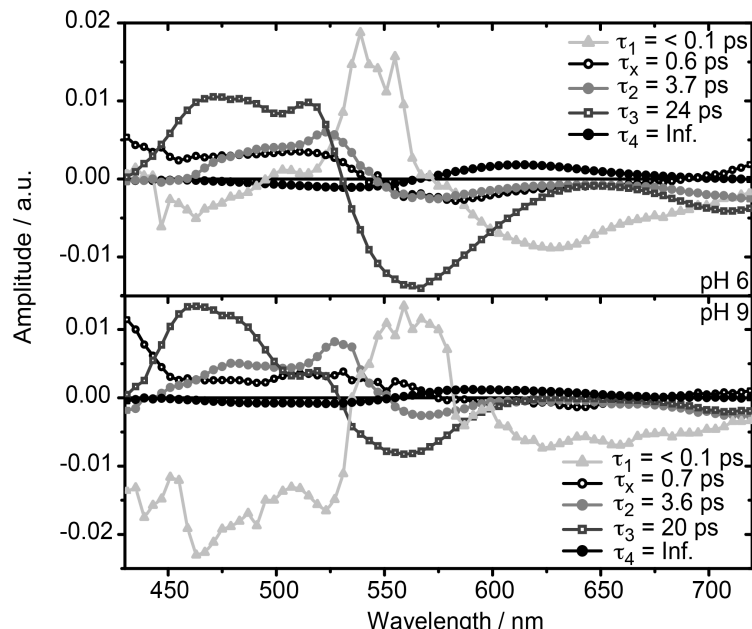


Fig. S7: Amplitude spectra (decay associated spectra, DAS) for GPR_{A178R} were calculated from the time constants in Tab. 1. Spectra for all five time constants at both pH values are very similar, which indicates that also the underlying processes are similar.

Interpretation of time constants from Tab. 1 and Fig. S7: Photoexcitation leads to the transition of the *all-trans* retinal into the first electronic excited state (S_1). The amplitude spectrum (Fig. S7) for τ_1 contains positive amplitudes for wavelengths around 550 nm and negative amplitudes at the red and the blue end of the recorded spectrum, suggesting the formation of an excited state population within τ_1 . τ_1 is therefore attributed to the motion of the initially generated wave packet out of the Franck-Condon region. The amplitude spectrum for τ_x contains contributions at shorter wavelength, suggesting an excited state relaxation that is not observed in GPR.

The time constants τ_2 and τ_3 can be assigned to the decay of the excited state population, due to their positive amplitude in the spectral range between 450 nm and 550 nm and negative amplitude in the spectral region of the stimulated emission. Therefore both time constants are attributed to the decay of the S_1 -state involving first a bond-stretching mode and later a torsional mode around the C13-C14 bond leading to the conical intersection with the ground state.

For GPR the time constant τ_3 is explained by a population decaying on a different way via a local energetic minimum on the S_1 potential energy surface that is separated from the conical intersection (CI) by a potential energy barrier (9). However the spectra for τ_2 and τ_3 are spectrally equal for GPR, while they differ in GPR_{A178R} , indicating that the S_1 potential energy surface is dramatically altered in GPR_{A178R} . Moreover the DAS for GPR_{A178R} are quite similar. Only a small shoulder of the absorption band around 500 nm is missing in the DAS of τ_2 at acidic pH, which can be attributed to the bathochromic shift at pH 6 compared to pH 9. These results show that the underlying mechanism for pH 6 and pH 9 is the same in GPR_{A178R} . In contrast to this for GPR the ratio of τ_2/τ_3 is altered with pH, suggesting that the faster reaction channel is more populated at alkaline pH. After crossing the S_1/S_0 conical intersection the molecule decays radiation less either to the initial state or to the K-like intermediate containing the retinal in its 13-*cis* conformation.

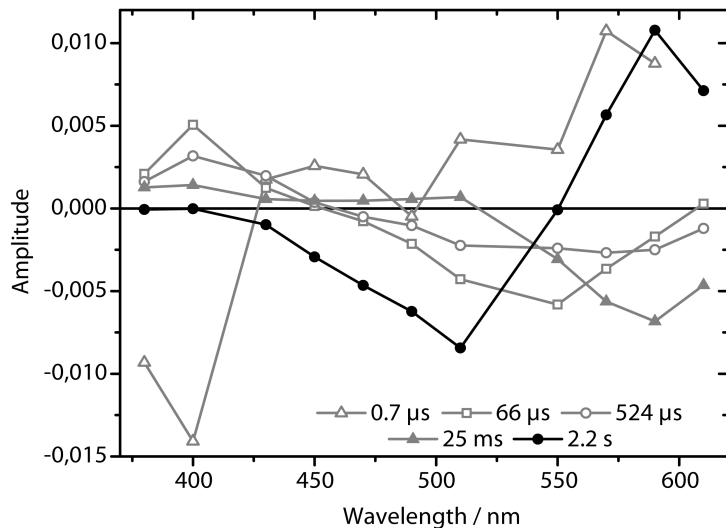


Fig. S8: Decay associated spectra of the time constants obtained from global fit for the transient flash photolysis data of GPR_{A178R} (Fig. 5, Tab. S2).

Tab. S2: Global fit analyses of the data set shown in Fig. 5.

	t_1	t_2	t_3	t_4	t_5
GPR / pH 9	69 μ s	1000 μ s	5200 μ s	44 ms	0.21 s
GPR_{A178R} / pH 9	0.7 μ s	66 μ s	524 μ s	25 ms	2.2 s

For GPR_{A178R} , five time constants are required. Data are compared to wild type GPR as published previously (10).

5. Supporting BLM Experiments

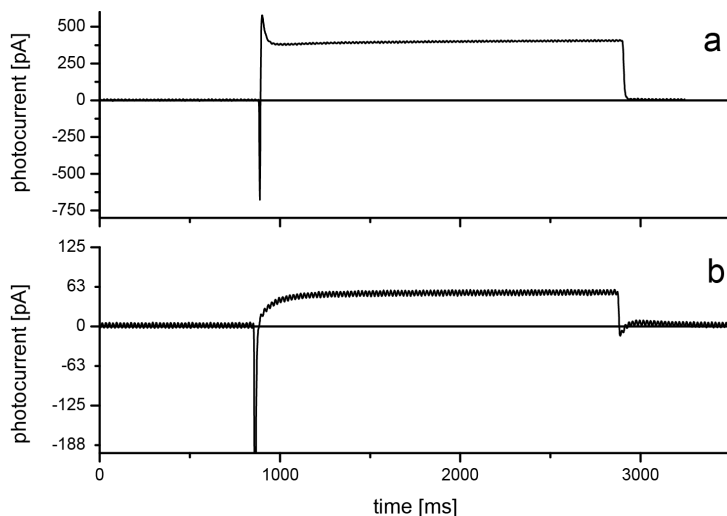


Fig. S9: Photocurrent of GPR (a) and GPR_{A178R} (b) reconstituted in liposomes (*E. coli* total lipid (1:25 mol/mol)) and attached to BLMs. Despite introducing the A178R mutation in the EF loop, which significantly affects photocycle kinetics, net transport of protons is observed under full illumination. The behavior of GPR under full illumination was essentially identical to that described by Friedrich and co-workers (11). A direct comparison with GPR reveals a smaller photocurrent, but further experiments would be required for a full characterization and explanation of its proton transport characteristics. All experimental details were similar to those described by Friedrich et al. (11). Experiment were performed at room temperature at pH7 in 20 mM HEPS buffer with 20 mM NaCl and in the presence of ionophores (5-10µM monensin; 3µM protonophore 1799 (2,6-dihydroxy)-1,1,1,7,7,7-hexafluoro-2,6-bis(trifluoro-methyl)heptane-4-one). Measurements were carried out under continuous illumination with yellow light (100 W Osram HBO mercury arc lamp).

Supporting References

1. Pardoen, J., C. Winkel, P. Muder, J. Lugtenburg, and 1984. Synthesis of retinals labeled at positions 14 and 15 (with C-13 and or H-2). *Recl. Trav. Chim. Pays-Bas* 103:135-141.
2. Sadhukhan, S., Y. Han, G. F. Zhang, H. Brunengraber, and G. P. Tochtrop. 2010. Using isotopic tools to dissect and quantitate parallel metabolic pathways. *J. Am. Chem. Soc.* 132:6309-6311.
3. Magoulas, G. E., S. E. Bariamis, C. M. Athanassopoulos, A. Haskopoulos, P. G. Dedes, M. G. Krokidis, N. K. Karamanos, D. Kletsas, D. Papaioannou, and G. Maroulis. 2011. Syntheses, antiproliferative activity and theoretical characterization of acitretin-type retinoids with changes in the lipophilic part. *Eur. J. Med. Chem.* 46:721-737.
4. McLean, N., A. Gansmuller, M. Concistre, L. Brown, M. Levitt, and R. Brown. 2011. Syntheses of C-13(2)-labelled 11Z-retinals. *Tetrahedron* 67:8404-8410.
5. Tanumihardjo, S. 2001. Synthesis of 10,11,14,15-C-13(4)- and 14,15-C-13(2)-retinyl acetate. *J. Labelled Compd. Radiopharmaceut.* 44:365-372.
6. Bergen, H., H. Furr, and J. Olson. 1988. Synthesis of tri-deuterated tetra-deuterated and penta-deuterated forms of Vitamin-A. *J. Labelled Compd. Radiopharmaceut.* 25:11-21.
7. Wada, A., Y. Ieki, S. Nakamura, and M. Ito. 2005. Palladium-catalyzed coupling reaction of an enol nonaflate with (vinyl)tributylstannanes and acetylenes: A highly stereoselective synthesis of 8,18-C-13(2)-labeled retinal. *Synthesis*:1581-1588.
8. Shi, L., M. A. Ahmed, W. Zhang, G. Whited, L. S. Brown, and V. Ladizhansky. 2009. Three-dimensional solid-state NMR study of a seven-helical integral membrane proton pump--structural insights. *J. Mol. Biol.* 386:1078-1093.
9. Lenz, M. O., R. Huber, B. Schmidt, P. Gilch, R. Kalmbach, M. Engelhard, and J. Wachtveitl. 2006. First steps of retinal photoisomerization in proteorhodopsin. *Biophys. J.* 91:255-262.
10. Hempelmann, F., S. Holper, M. K. Verhoeven, A. C. Woerner, T. Kohler, S. A. Fiedler, N. Pfleger, J. Wachtveitl, and C. Glaubitz. 2011. His75-Asp97 cluster in green proteorhodopsin. *J. Am. Chem. Soc.* 133:4645-4654.
11. Friedrich, T., S. Geibel, R. Kalmbach, I. Chizhov, K. Ataka, J. Heberle, M. Engelhard, and E. Bamberg. 2002. Proteorhodopsin is a light-driven proton pump with variable vectoriality. *J. Mol. Biol.* 321:821-838.